

## Revision 2

# Kobellite homologues from the Boliden Au-Cu-(As) deposit, Sweden: jigsaw patterning via nanoscale intergrowths in chessboard structures

CRISTIANA L. CIOBANU<sup>1,\*</sup>, ASHLEY D. SLATTERY<sup>2</sup>, NIGEL J. COOK<sup>1</sup>, BENJAMIN P. WADE<sup>2</sup>, KATHY EHRIG<sup>3,1</sup>, THOMAS WAGNER<sup>4</sup>, WENYUAN LIU<sup>5</sup>

<sup>1</sup> School of Chemical Engineering, The University of Adelaide, Adelaide, SA 5005, Australia

<sup>2</sup> Adelaide Microscopy, The University of Adelaide, Adelaide, SA 5005, Australia

<sup>3</sup> BHP Olympic Dam, 10 Franklin Street, Adelaide SA 5000, Australia

<sup>4</sup> Institute of Applied Mineralogy and Economic Geology, RWTH Aachen University, Germany

<sup>5</sup> Zijin School of Geology and Mining, Fuzhou University, Fuzhou 350108, China

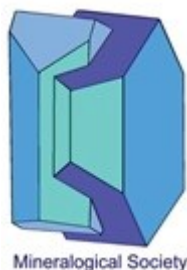
---

### Abstract

Sulphosalt assemblages in a specimen from the Boliden Au-Cu-(As) deposit (northern Sweden) comprise micron- to nanoscale intergrowths of Se-rich izoklakeite and tintinaite with average formulae and calculated homologue number (N) given as:  $(\text{Cu}_{1.88}\text{Fe}_{0.18})_{2.06}(\text{Pb}_{22.92}\text{Ag}_{1.47}\text{Cd}_{0.01}\text{Zn}_{0.01})_{24.41}(\text{Sb}_{13.12}\text{Bi}_{8.69})_{21.8}(\text{S}_{50.19}\text{Se}_{6.43}\text{Te}_{0.12})_{56.73}$ ,  $N=3.83$ , and  $(\text{Cu}_{1.31}\text{Fe}_{0.74})_{2.05}(\text{Pb}_{10.58}\text{Ag}_{0.18}\text{Cd}_{0.05}\text{Zn}_{0.02})_{10.83}(\text{Sb}_{10.2}\text{Bi}_{5.23})_{15.43}(\text{S}_{32.22}\text{Se}_{2.46})_{34.7}$ ,  $N=2.05$ , respectively. Tintinaite coexists with (Bi, Se)-rich jamesonite. High-angle annular dark field scanning transmission electron microscopy (HAADF STEM) imaging reveals chessboard structures comprising PbS and SnS modules with the number of atoms in the octahedral (M) sites counted as:  $n_1=18$  and  $n_2=8$  for tintinaite, and  $n_1=30$  and  $n_2=16$  for izoklakeite. Homologue number can be calculated using the formula:  $N=(n_1/6)-1$  and  $N=n_2/4$  for PbS and SnS modules giving  $N_{\text{Ti}}=2$  and  $N_{\text{Iz}}=4$ . A new  $N=3$  homologue, defined by  $n=12$  and  $n=24$  SnS and PbS modules, respectively, is identified as single or double units within areas with intergrowths between kobellite and izoklakeite. HAADF STEM imaging also reveals features attributable to lone electron pair micelles within the Sb-rich kobellite homologues. Atomic-resolution EDS STEM chemical mapping of Pb-Bi-Sb-sulphosalts shows a correlation with crystal structural modularity. The maps also highlight sites in the SnS modules of

---

\* Corresponding author. e-mail address: cristiana.ciobanu@adelaide.edu.au



This is a 'preproof' accepted article for Mineralogical Magazine. This version may be subject to change during the production process.  
DOI: 10.1180/mgm.2024.41

tintinaite in which  $Sb > Bi$ . Coherent nanoscale intergrowths between tintinaite and izoklakeite define jigsaw patterns evolving from chessboard structures and are considered to have formed during co-crystallisation of the two phases. Displacement textures and crosscutting veinlets (a few nm in width) are interpreted as evidence for superimposed syn-metamorphic deformation and are associated with the redistribution of Bi and Se. Imaging and mapping using HAADF STEM techniques is well suited to characterisation of Pb-Sb-Bi-sulphosalt phases, offering largely untapped potential to unravel the evolution of chessboard structures with applications across mineralogy but also extending into allied fields.

**Keywords:** HAADF STEM; nanoscale intergrowths; kobellite homologous series; tintinaite, izoklakeite; Boliden.

---

## Introduction

The kobellite homologous series is described by the formula  $(Cu,Fe)_2M_{10N+6}S_{11N+13}$  for a 4 Å repeat where  $M = Pb, Bi, Sb$ ;  $N =$ homologue number (Makovicky and Mumme, 1986; Zakrzewski and Makovicky, 1986). Natural phases of the kobellite homologous series include kobellite and tintinaite with  $N = 2$ , and giessenite and izoklakeite with  $N = 4$ .

Tintinaite (Sb-rich) and kobellite (Bi-rich) are isostructural and form a continuous solid solution pair with general formula:  $(Cu_{2-x}Fe_x)[Pb_{10-2z+x}(Ag,Cu)_z(Sb_{1-y}Bi_y)_{16+z-x}]_{26}S_{35}$ ;  $0 < x < 1$ ;  $0 < y < 0.67$ ;  $0 < z < 0.54$  (Moëlo *et al.*, 1995). Tintinaite from the type locality (TL) Tintina Mine, Yukon, was defined as the Sb-pure equivalent of kobellite from TL Hvena, Sweden (Harris *et al.*, 1968; Moëlo *et al.*, 1984). The two species have space group *Pnmm* and cell parameters:  $a = 22.30$  Å;  $b = 34.00$  Å;  $c = 4.04$  Å for TL tintinaite (Harris *et al.*, 1986), and  $a = 22.62$  Å;  $b = 34.08$  Å;  $c = 4.04$  Å for TL kobellite (Nuffield, 1948).

Izoklakeite, ideally  $[(Cu,Fe)_2Pb_{26.5}(Sb,Bi)_{19.5}S_{57}]$ , is orthorhombic (space group *Pnmm*;  $a = 34.07$  Å,  $b = 37.98$  Å,  $c = 4.072$  Å (specimen from Vena, Sweden; Zakrzewski and Makovicky, 1986) whereas its Bi-dominant analogue giessenite, ideally  $[(Cu,Fe)_2Pb_{26.4}(Bi,Sb)_{19.6}S_{57}]$ , is monoclinic (space group *P2<sub>1</sub>/n*  $a = 34.34$  Å;  $b = 38.05$  Å,  $c = 4.06$  Å,  $\beta = 90.33^\circ$  (specimen from Bjorkåsen, Norway; Makovicky and Karup-Møller, 1986). Although no Sb-pure izoklakeite has been described, Bi-rich izoklakeite specimens with orthorhombic symmetry are documented from Lake Zervreila, (Iz:Gie ratio 40:60; Armbruster and Hummel, 1987) and Gutaishan, China (Iz:Gie ratio 35:65; Li *et al.*, 2019). The general formula for a quasi-solid solution between izoklakeite and giessenite was given as:  $(Cu_{2-x}Fe_x)[Pb_{26-2z+x}(Ag,Cu)_z(Sb_{1-y}Bi_y)_{20+z-x}]_{46}S_{57}$ ;  $0 < x < 1$ ;  $0.44 < y < 0.85$ ;  $0 < z < 2.2$  (Moëlo *et al.*, 1995), even though the exact Sb:Bi ratio at which the symmetry changes is unknown (Moëlo *et al.*, 2008).

Distinguishing among these sulphosalt phases, and also compositionally similar but structurally unrelated phases such as jaskólskiite ( $\text{Cu}_x\text{Pb}_{2+x}(\text{Sb},\text{Bi})_{2-x}\text{S}_5$  ( $x\sim 0.15$ ; Zakrzewski, 1984; Makovicky and Nørrestam, 1985), or jamesonite ( $\text{FePb}_4\text{Sb}_6\text{S}_{14}$ ) (Niizeki and Buerger, 1957) can be difficult based solely on compositional data (e.g., electron probe microanalysis; EPMA). Unequivocal identification from EPMA data is impossible if the phases are intergrown at the sub-micron scale.

A prior study (Li *et al.*, 2019) demonstrated the utility of the high-angle annular dark field scanning transmission electron microscope (HAADF STEM) technique for visualising the crystal structures of coexisting kobellite and izoklakeite based on their characteristic modular structures. Here, we characterize intergrowths of Sb-rich kobellite homologues, modular minerals that extend down to the nanoscale and thus yield compositions at the scale of the microprobe beam that cannot be readily reconciled with one species or the other.

Boliden is a Paleoproterozoic metamorphosed massive sulphide deposit in the Skellefte district of northern Sweden with characteristics interpreted as an ancient analogue to a modern high-sulphidation environment (Weihed *et al.*, 1996). The deposit was known for its high gold grades (average 15 ppm), massive arsenopyrite orebodies, and highly complex ore mineral assemblages (Grip and Wirstam, 1970; Wagner and Jonsson, 2001). An important part of the deposit is represented by sulphosalt-rich veins that host, alongside kobellite, a variety of other ore minerals including several Se-bearing sulphosalts (e.g., tetrahedrite, bournonite, boulangerite, meneghinite), Bi-selenides and -tellurides (tellurobismuthite, tetradymite and laitakarite), Hg-rich gold-silver alloys, gudmundite, and native bismuth (Ödman, 1941; Grip and Wirstam, 1970; Wagner and Jonsson, 2001; Wagner *et al.*, 2007).

Selenium-rich kobellite has been previously reported from Boliden (Moëlo *et al.*, 1984 (reanalysis of a sample from Harris *et al.*, 1968); Wagner and Jonsson, 2001; Mumme *et al.*, 2013). Whereas the crystal structure of this Se-rich kobellite (Mumme *et al.*, 2013) differs only in minor ways from that determined for kobellite by Mieke (1971), the Sb concentration can vary in Boliden kobellite. A Sb/(Bi+Sb) ratio of  $\sim 0.5$  is reported by Moëlo *et al.* (1984) and Mumme *et al.* (2013) and  $\sim 0.6$  (Wagner and Jonsson, 2001). On this basis, the Boliden kobellite reported by Wagner and Jonsson (2001) will hereafter be referred to as tintinaite.

This contribution describes co-existing Se-rich kobellite homologues (izoklakeite and tintinaite) that form micro- to nanoscale intergrowths in a specimen from the sulphosalt-rich veins at Boliden. By comparison with documented occurrences worldwide, we show these are among the most Sb-rich varieties that also contain Bi yet reported. We discuss the nature of the nanoscale intergrowths and show the presence of both primary and secondary textures. The primary intergrowths lead to formation of a new kobellite homologue during sulphosalt co-crystallization, whereas the secondary textures record nanoscale remobilization of Bi and Se during vein shearing. We aim to show how

HAADF STEM imaging of modular structures is an appropriate tool to validate their building blocks and provide atomic-scale insights into formation of new phases as well as the primary versus secondary/overprinting origin of observed intergrowths.

### **Analytical methodology**

The investigated sample (specimen 1061) originates from the Boliden Mineral AB collection that formed the basis of the first description of the deposit by Ödman (1941). The sample was collected from the 250 m level E in the mine, in room 28 about 213-216 meters away from the western part. Ore samples were mounted, polished, and examined under reflected light and in backscatter electron mode using an FEI Quanta 450 Field Emission Gun scanning electron microscope equipped with a silicon-drift energy-dispersive X-ray spectrometer (Adelaide Microscopy, The University of Adelaide).

Quantitative compositional data (spot analyses) and element maps were obtained using a Cameca SX-Five electron probe microanalyser in the same laboratory. The instrument runs PeakSite v6.5 software for microscope operation, and Probe for EPMA software for data acquisition and processing. The instrument is equipped with five tunable wavelength-dispersive spectrometers and was operated at 20 kV and 20 nA with a focussed beam. X-ray lines were as follows: S ( $K\alpha$ ), Pb ( $M\alpha$ ), Se ( $L\alpha$ ), Te ( $L\alpha$ ), Bi ( $M\alpha$ ), As ( $L\alpha$ ), Fe ( $K\alpha$ ), Cu ( $K\alpha$ ), Mn ( $K\alpha$ ), Ag ( $L\alpha$ ), Zn ( $K\alpha$ ), Sb ( $L\alpha$ ), Cd ( $L\alpha$ ). All standards used were from P&H and Associates: galena for Pb and S, chalcopyrite for Cu and Fe, synthetic guanajuatite ( $Bi_2Se_3$ ) for Bi and Se, gallium arsenide for As, galena for Pb, rhodonite for Mn, silver telluride for Ag, HgTe for Te, sphalerite for Zn, stibnite for Sb, and greenockite for Cd. On-peak count times were 20 s on peak for all elements except Pb and S (15 s). Due to the complexity of off peak interferences, traditional two point background analysis was initially acquired (20 s high and 20 s low), then through a function of the Probe for EPMA software these were turned into multipoint backgrounds utilising an exponential curve for background fitting. On peak interferences were corrected using a range of standards in Probe for EPMA. Average minimum detection limits (99% C.I. in wt.%) were 0.008 for S, 0.05 for Pb and Ag, 0.04 for Bi and Cd, 0.03 for Se, Te, As, Cu, and Zn, and 0.02 for Te, Sb, Fe, and Mn. Qualitative X-ray mapping utilised the same instrument were acquired using Probe Image at settings of 20 kV and 200 nA at a pixel resolution of  $\sim 1 \mu m$ . Pixel dwell time was set to 2000 ms for enhanced sensitivity. Intensity maps were then coloured using Surfer 10® software distributed by Golden Software.

Additional element mapping was undertaken by laser ablation inductively coupled plasma mass spectrometry (LA-ICP-MS) using a RESolution-LR 193 nm excimer laser attached to an Agilent 7900x Quadrupole ICP-MS. The following suite of isotopes were measured:  $^{34}S$ ,  $^{57}Fe$ ,  $^{59}Co$ ,  $^{60}Ni$ ,  $^{65}Cu$ ,  $^{75}As$ ,  $^{77}Se$ ,  $^{107}Ag$ ,  $^{121}Sb$ ,  $^{125}Te$ ,  $^{197}Au$ ,  $^{206}Pb$ , and  $^{209}Bi$ . LA-ICP-MS trace element maps were

generated by ablating sets of parallel line rasters in a grid across the sample surface. A square laser beam profile was used throughout with spot size varying between 11 and 16  $\mu\text{m}$  to provide adequate spatial resolution for each map. Spacings between adjacent trenches and laser beam scan speed were modified to match spot size. Laser fluence was  $\sim 3.5 \text{ J/cm}^2$  using a repetition rate of 10 Hz. A 10 s background measurement was acquired before the ablation of each trench, followed by a 20 s delay after ablation. Two 74  $\mu\text{m}$ -diameter spot analyses were made on STDGL3 and GSD-1G reference materials at 10 Hz before and after each map. All LA-ICP-MS trace element maps were processed with Iolite software.

Thinned <100 nm-thick foils for nanoscale investigation were prepared *in-situ* from the surface of a polished mount attached to a copper grid using focused ion beam – SEM techniques. This was carried out on a FEI-Helios nanoLab dual focused ion beam and scanning electron microscope (FIB-SEM) at Adelaide Microscopy, The University of Adelaide. Extraction and thinning procedures followed Ciobanu *et al.* (2011).

HAADF STEM imaging and EDS analysis reported here were performed using an ultra-high resolution, probe-corrected, FEI Titan Themis S/TEM in the same laboratory and previously used for imaging sulphosalts structures (e.g., Ciobanu *et al.* 2016; Li *et al.*, 2019). This instrument is equipped with a X-FEG Schottky source and Super-X EDS geometry. The Super-X EDS detector provides geometrically symmetric EDS detection with an effective solid angle of 0.8 sr. Probe correction delivered sub-Ångstrom spatial resolution and an inner collection angle greater than 50 mrad was used for HAADF imaging with a Fischione detector. Image acquisition, including drift-corrected frame integration package (DCFI) and processing, was performed using both DigitalMicrograph™ and Thermo-Scientific Velox software. Various filters were used to eliminate noise. EDS mapping was performed using Thermo-Scientific Velox software, which utilizes standard Cliff-Lorimer quantification and included absorption correction optimized for both the Super-X detector geometry and also the effect of sample holder shadowing for the double-tilt Super-X holder used.

Diffraction indexing was performed using Winwulff© (JCrystalSoft) software. Data stored in the American Mineralogist Crystal Structure Database (<http://rruff.geo.arizona.edu/AMS/amcsd.php>). Crystal structure models were generated in CrystalMaker® and image simulations using STEM for xHREM™ (v4.1) software.

## Results

### *Specimen petrography – micron-scale characterisation*

Both analysed polished blocks (1061 and 1061a) feature lamellar intergrowths between Pb-Sb-Bi-sulphosalts, identified as tintinaite and izoklakeite, and Bi-Pb chalcogenides which are readily

distinguishable from the sulphosalts by their colour and brightness in reflected light (Fig. 1a-c). The bismuth minerals are associated with minor chalcopyrite, either interstitial within, or at the margins of the sulphosalts, and with pyrite, a major component of polished block 1061 (Fig. S1, Supplementary Material). The three areas selected for nanoscale study (all in polished block 1061a) targeted contacts between acicular tintinaite lamellae and the Bi-Pb chalcogenide and the mutual contacts between the two sulphosalt species (Fig. 1d-f). Bi-Pb chalcogenide species are dominated by a new member of the aleksite series with the formula  $\text{PbBi}_6(\text{Te,Se})_6(\text{S,Se})_4$  calculated from electron probe microanalysis. The composition and crystal structure of this phase will be reported in detail elsewhere.

LA-ICP-MS trace element maps (polished block 1061) show that the sulphosalts concentrate minor Ag and Cd, whereas Se is a major component of the Bi-chalcogenide (Fig. 2a). A pyrite grain with corroded margin at the mutual boundary with sulphosalts displays a Co-enriched rim but patchy distribution of As and Ni. Specks of relatively high Au concentration occur across the boundary between pyrite and the sulphosalt. Such textures are indicative of small-scale trace element remobilisation during an overprinting event. This is also illustrated by the presence of laitakarite,  $[(\text{Bi}_4(\text{Se,S})_3)]$ , among other Bi-chalcogenide species from the tetradymite series, which occurs along trails crosscutting pre-existing phase boundaries (e.g., between sulphosalt and aleksite series species, as seen on BSE images and EPMA maps; Fig. 2b, c). Fine-scale intergrowths between izoklakeite and tintinaite are readily seen on EPMA element maps for Pb (Fig. 2d).

### *Chemical composition*

Compositional data for the two sulphosalts was obtained from both polished blocks. Mean compositions of izoklakeite and tintinaite and are given in Tables 1, and 2-3, respectively. The complete EPMA datasets for kobellite homologues, and associated (Bi, Se)-rich jamesonite are compiled as Tables S1, S2 and S3 (Supplementary Materials). A selection of published data for kobellite homologues used for comparison are given in Table S4 (Supplementary Materials).

To achieve an optimal correlation between micron-and nanoscale characterisation, electron probe microanalysis of sample 1061a was carried out in areas immediately adjacent to the site of FIB cutting (Table 3). Analysis spots along short profiles are marked on Fig. 1d-f.

The ideal endmembers of the two homologues as defined by Zakrzewski and Makovicky (1986) give a range of  $M^{2+}(\text{Pb,Cd,Zn})$  relative to  $M^{3+}(\text{Sb,Bi})$  ratios (cations with octahedral and prismatic coordination) correlated to the presence of atoms in tetrahedral coordination ( $T=\text{Cu}^+, \text{Fe}^{2+}$ ) by the formula:

$$N_{\text{homologue}} = x \frac{6M^{2+} + 3M^{3+}}{4M^{3+} - M^{2+}} + (1-x) \frac{5M^{2+} + 2M^{3+}}{4M^{3+} - M^{2+}}, \text{ where } x = \frac{T^+}{(T^+ + T^{2+})} \text{ and } (1-x) = \frac{T^{2+}}{(T^+ + T^{2+})}.$$

For the sake of simplicity,  $\text{Ag}^+$  is included in the  $\text{M}^{2+}$  site and only  $\text{Cu}^+$  is considered.

The  $\frac{\text{M}^{2+}}{\text{M}^{3+}}$  ratio is higher for  $x=0$  than for  $x=1$  (0.86 and 0.63 for kobellite-tintinaite, 1.56 and 1.3 for izoklakeite). The lowest ratio is obtained for  $T=0$ , where  $\frac{\text{M}^{2+}}{\text{M}^{3+}} = \frac{8N-8}{2N+14}$ , i.e., 0.44 for  $N=2$  (kobellite or tintinaite) and 1.09 for  $N=4$  (izoklakeite). For  $N$  calculation we used the substitution:  $\text{Ag}^+ + (\text{Sb}, \text{Bi})^{3+} \rightarrow 2 \text{Pb}^{2+}$ , as considered for formula calculation (Moëlo *et al.* 1995).

Izoklakeite has a mean composition  $\text{Iz}_{60}\text{Gie}_{40}$  (Table 1) with the empirical formula:  $(\text{Cu}_{1.88}\text{Fe}_{0.18})_{2.06}(\text{Pb}_{22.92}\text{Ag}_{1.47}\text{Cd}_{0.01}\text{Zn}_{0.01})_{24.41}(\text{Sb}_{13.12}\text{Bi}_{8.69})_{21.8}(\text{S}_{50.19}\text{Se}_{6.43}\text{Te}_{0.12})_{56.73}$ . This corresponds to a  $\text{Pb}(\text{Ag}, \text{Cd}, \text{Zn})$ -depleted,  $(\text{Sb}, \text{Bi})$ -enriched composition relative to the ideal  $N=4$  homologue,  $(\text{Cu}, \text{Fe})_2\text{Pb}_{26}(\text{Sb}, \text{Bi})_{20}\text{S}_{57}$ , with substitution factor  $x=1$  (Zakrzewski and Makovicky, 1986). The mean homologue number  $N$  is 3.83 using calculations based on 105 a.p.f.u (Table 4).

The mean tintinaite composition is  $\text{Tti}_{66}\text{Kbl}_{34}$  with the empirical formula:  $(\text{Cu}_{1.31}\text{Fe}_{0.74})_{2.05}(\text{Pb}_{10.58}\text{Ag}_{0.18}\text{Cd}_{0.05}\text{Zn}_{0.02})_{10.83}(\text{Sb}_{10.2}\text{Bi}_{5.23})_{15.43}(\text{S}_{32.22}\text{Se}_{2.46})_{34.7}$  and calculated  $N=2.05$  (Tables 2 and 4). Tintinaite is richer in  $\text{Pb}(\text{Ag}, \text{Cd}, \text{Zn})$  and slightly poorer in  $(\text{Sb}, \text{Bi})$  than the ideal  $N=2$  homologue,  $(\text{Cu}, \text{Fe})_2\text{Pb}_{10}(\text{Sb}, \text{Bi})_{16}\text{S}_{35}$ , with substitution factor  $x=1$  (Zakrzewski and Makovicky, 1986), thus opposite to the trend shown by izoklakeite.

The Sb-rich sulphosalt occurring as the darkest lamellae on BSE images from FB area 3 (Fig. 1f) contains Fe and was identified as jamesonite  $(\text{Fe}_{0.99}\text{Cu}_{0.01})_{1.00}(\text{Pb}_{3.89}\text{Cd}_{0.03})_{3.91}(\text{Sb}_{5.14}\text{Bi}_{1.03})_{6.17}(\text{S}_{13.14}\text{Se}_{0.78})_{13.92}$  (Table S4 Supplementary Materials). Notably, Se is present in this third sulphosalt, albeit at a lower concentration (2.81 wt.%) than in izoklakeite (4.82 wt.%) or tintinaite (3.3 wt.%).

There are, however, subtle compositional variations within each sulphosalt from the two polished blocks and, for tintinaite, also between the three analysed areas (Fig. 3; Tables 1-3; Tables S1 and S2, Supplementary Materials). Both izoklakeite and tintinaite show a slight relative depletion in  $\text{Pb}(\text{Ag}, \text{Cd}, \text{Zn})$  in the pyrite-rich sample (1061) compared to the sulphide-poor sample (1061a). Tintinaite coexisting with izoklakeite (area 2, 1061a) is lowest in  $\text{Pb}(\text{Ag}, \text{Cd}, \text{Zn})$ , whereas tintinaite coexisting with  $(\text{Bi}, \text{Se})$ -rich jamesonite is lowest in  $\text{Sb}+\text{Bi}$  but highest in  $\text{Pb}(\text{Ag}, \text{Cd}, \text{Zn})$  (Fig. 3). Izoklakeite displays a more marked  $\text{Pb}(\text{Ag}, \text{Cd}, \text{Zn})$  variation between the two samples than tintinaite.

### *Nanoscale characterisation*

Three areas of the Boliden specimen were investigated in four S/TEM foils obtained from polished block 1061a as marked on Figure 1a: one (foil #1) from area 1, two (foils #2 and #3) from area 2, and one (foil #4) from area 3 (Figure 4a-d). Contacts between tintinaite and the  $\text{Pb}$ - $\text{Bi}$ -chalcogenide are sharp (Fig. 4a, b), with a thin sliver of Sb-rich Bi sulphosalt, a few  $\mu\text{m}$ -wide observed in foil #1 which is obtained from the area where no  $\mu\text{m}$ -scale lamellae of tintinaite are identified. Foils obtained across the contacts between tintinaite and izoklakeite (Fig. 4c, d) display intergrowths between the two

/

phases, and feature  $\mu\text{m}$ - to sub- $\mu\text{m}$ -scale patches of the Pb-Bi-chalcogenide. EDS STEM maps across the three phases in foil #1 show a relative enrichment of Ag in tintinaite and the Pb-Bi-chalcogenide, whereas the Sb-rich Bi-sulphosalt is also enriched in Fe (Fig. 4e), consistent with jamesonite. Selenium is concentrated within the Pb-Bi-chalcogenide.

Nanoscale intergrowths between tintinaite and izoklakeite are widespread along the direct contacts between the two phases (Fig. 5). Typically, the intergrowths consist of lamellae of one species within the other forming rhythmic banding within fine-grained aggregates (Fig. 5a-c). The banding is however irregular, with rhythms that change across the same grain, and with lamellae thickness that varies from a few nm to several tens of nm in width. The Pb-Bi-chalcogenide is embayed into the sulphosalt aggregates (Fig. 5b). Sharp changes in banding patterns are observed across grain contacts (Fig. 5c). STEM EDS maps of sulphosalt intergrowths show significant compositional changes in some elements, particularly  $\text{Sb} > \text{Pb}$  or  $\text{S} > \text{Se}$  in tintinaite versus izoklakeite, whereas the variation in Bi is more subtle (Fig. 5d, e). Izoklakeite is richer in minor Ag but poorer in Fe relative to tintinaite. Clusters of Bi-Se nanoparticles (NPs) decorate the margins of tintinaite lamellae which are either truncated or displaced by fractures (Fig. 5e).

#### *Chemical structural modularity: the main building modules in tintinaite and izoklakeite*

PbS and SnS modules are readily identified on the [001] zone axis of tintinaite and izoklakeite (Fig. 6a-d). These are recognised on HAADF STEM images as blocks with the number of heavy atoms M (bright dots on images) counted as:  $n_1=18$  and  $n_2=8$  for tintinaite, and  $n_1=30$  and  $n_2=16$  for izoklakeite (overlays on Fig. 6a, c). Using the formulae  $\text{M}_{6(N+1)}\text{S}_{7N+9}$  and  $\text{M}_{4N}\text{S}_{4(N+1)}$  ( $\text{M}=\text{Bi}, \text{Sb}, \text{Pb}$ ) (Makovicky and Mumme, 1986; Zakrzewski and Makovicky, 1986), we can calculate the homologue number N from the M sites as:  $N=n_1/6-1$  and  $N=n_2/4$  for PbS and SnS modules giving  $N_{\text{Kbl}}=2$  and  $N_{\text{Lz}}=4$ . The atomic arrangements for the larger SnS modules are shown as given by Li *et al.* (2019) and Makovicky and Mumme (1986).

The crystal structure models show a very good correlation with the STEM simulations and atomic-scale images for the two sulphosalts (Fig. 7). The structures (Miehe, 1971; Makovicky and Mumme, 1985) consist of PbS and SnS modules (referred to as rods in earlier descriptions of Makovicky and Mumme, 1985; Zakrzewski and Makovicky, 1986) that alternate on both *a* and *b* directions (highlighted by overlays on crystal models, STEM simulations and images in Fig. 7). Tetrahedral-coordinated cations ( $\text{T}=\text{Cu}, \text{Fe}$ ) are nested at the module interfaces. The HAADF STEM images show patterns of dark lines, particularly visible through the centre of the SnS modules in izoklakeite. These correspond to weaker/longer Sb(Bi)-S bonds between adjacent polyhedra.

High-resolution EDS STEM element maps and their overlays show a good match with atom-fill models for the two sulphosalts (Figs. 8, 9, and Supplementary Materials Figures S2 and S3). Overlays

of Sb-Pb-Bi-Fe maps and crystal model for tintinaite show an excellent correlation with the two building modules (Fig. 8a). The distribution of Fe in the tetrahedral sites flanking the corners of the SnS module and in the kinks of the PbS module are very well depicted for tintinaite. Overlays of Sb-Pb-Bi maps with the HAADF STEM image also reproduce the two modules, albeit with less accuracy than for tintinaite (Fig. 8b). Nonetheless, the distribution of SnS modules is well resolved for izoklakeite.

In closer detail, the EDS STEM element maps for Pb, Sb, Bi and Fe in tintinaite show the distribution of these elements throughout the structure whereby four Bi/Sb sites are at centre of the SnS modules; these are surrounded by Pb atoms (Fig. 9a). Taking the crystal model for the asymmetric unit cell from Miehe (1971), there are seven Bi/Sb sites of which two have 0.5:0.5 ratios, whereas the others, except site #1 where Sb is twice as much as Bi (0.33:0.67), have occupancies in which Bi>Sb (Fig. 9b). The map for Sb suggests, however, that occupancy is Sb>Bi for sites #3, 4 and 5 (Fig. 9a). This agrees with the higher tintinaite component in Boliden N=2 kobellite homologue compared with the specimen studied by Miehe (1971); 66 mol.% and 44 mol.% tintinaite, respectively.

#### *Nanoscale intergrowths and defects in tintinaite-izoklakeite*

Considering that  $b_{\text{Kbl} \sim \text{Ti}}$  and  $a_{\text{Iz}}$  are equal ( $\sim 34 \text{ \AA}$ ), coherent syntactic intergrowths along these directions are commonly formed (Fig. 10a-c). In some cases, however, the boundaries between such intergrowths show stepwise displacements with small-scale re-shaping and are accompanied by protrusion of Bi-rich stringers (Fig. 10a). Likewise, the boundaries between grains featuring rhythmic intergrowths of variable width are curvilinear, with small adjustments along the  $(010)_{\text{Ti}}$  and  $(100)_{\text{Iz}}$  planes (Fig. 10b, c). At higher magnification, the adjustments are illustrated by misorientations in the building modules (Fig. 10d) and swells along boundaries (Fig. 10e), as well as loops and kinks of the smallest-scale arrays of one species within another (Fig. 10f). Defects along  $(100)$  planes in izoklakeite show a doubling of the building modules and their displacements at the edges of the defects or along mutual contacts between the two sulphosalts (Fig. 10g, h).

The match between the values of  $b_{\text{Kbl}}$  and  $a_{\text{Iz}}$  at  $\sim 34 \text{ \AA}$  allows formation of intergrowths between tintinaite and izoklakeite (Fig. 11). The alternating PbS and SnS modules that form a zig-zag line along  $(100)_{\text{Ti}} // (010)_{\text{Iz}}$  planes are shown on the model in Figure 11a. The change between tintinaite and izoklakeite along  $a_{\text{Ti}}$  and  $b_{\text{Iz}}$  is achieved by increasing the width of these modules whereas their heights remain constant ( $\sim 17 \text{ \AA}$ ). The HAADF STEM image shows a perfect match with the model (compare Fig. 11a and b). Oblique contacts between  $[001]_{\text{Ti}}$  and  $[001]_{\text{Iz}}$  are often observed (Fig. 11c). In this case the alignment between  $(010)_{\text{Ti}}$  and  $(100)_{\text{Iz}}$  planes features small scale areas of mismatch, recognisable by misfit of the two types of modules and their respective morphologies (Fig. 11d, e).

Formation of defects and nano-to microfractures are both associated with element remobilisation and accompany this type of low-angle misfit between the two sulphosalts (see below).

The second most common type of modular intergrowths within either tintinaite or izoklakeite is observed along planes from the  $\langle 110 \rangle$  family (Fig. 12). Single arrays of smaller PbS modules along  $(1\bar{1}0)$  planes in izoklakeite (Fig. 12a) can be interpreted as modules corresponding to an N=3 homologue (N3), i.e., from  $n_1=24$  and  $n_2=12$  defined by PbS and SnS modules, albeit with corner-sharing of atoms between PbS modules along  $(100)_{Iz}$  (Fig. 12b). Arrays of thicker SnS modules along  $(1\bar{1}0)$  planes in tintinaite (Fig. 12c) can be interpreted as two PbS modules of the N3 homologue alternating with SnS modules of tintinaite (Fig. 12d). Likewise, module disorder and formation of the N3 homologue are observed when the intergrowths comprise changes in thickness or branching between arrays of different orientations (Fig. 12e-h).

A range of textures crosscutting the main crystal structural motifs of the two sulphosalts and leading to redistribution of Bi and Se are also depicted (Fig. 13). Modifications of the PbS module in both izoklakeite or tintinaite, e.g., giving them a S-shaped or irregular appearance, are present as single defects (Fig. 13a-c), or occur along nanofractures displaying Bi enrichment (Fig. 13d). Some lamellae ( $\sim 26$  Å-wide) feature building modules which, although syntactic with host tintinaite, are different to kobellite homologues (Fig. 13e). These are associated with localised enrichment in Bi and Se, and depletion in Sb (Fig. 13f).

## Discussion

### *Compositional variation in kobellite homologues: comparison with other occurrences*

The compositional variation observed in species from the tintinaite-kobellite and izoklakeite-giessenite series from previously published studies spanning a range of magmatic-hydrothermal and metamorphosed deposits (Fig. 14; Table S3, Supplementary Materials) reflects the ability of modular structures to adapt to changes in physical and chemical parameters of fluids during ore formation.

The Boliden izoklakeite,  $Iz_{\sim 60}Gie_{\sim 40}$ , is richer in Sb (highest Iz component) than all previously published data (Table 1, 4 and Table S3, Supplementary Materials), including the type specimen from Izok Lake, Canada (Harris *et al.*, 1986) with composition  $Iz_{53}Gie_{47}$ .

Likewise, the average tintinaite composition,  $Tti_{66}Kbl_{34}$ , shows this is also rich in Sb, comparable to Pedra Luz,  $Tti_{65}Kbl_{35}$  (Moëlo *et al.*, 1995), and higher than the  $Tti_{51}Kbl_{39}$  composition from Boliden given by Wagner and Jonsson (2001) (Tables 2, 4 and Table S3, Supplementary Materials). The Tti:Kbl ratio in tintinaite analysed here shows a Tti:Kbl range between 64:36 and 69:31, clearly representing the highest Sb-rich composition reported if we exclude the TL tintinaite which lacks any Bi (Harris *et al.*, 1986). Previously reported data for the N=2 homologue considered kobellite from

Boliden have Tti:Kbl ratios midway through the series, i.e., 50:50 (Moëlo *et al.*, 1984) and 52:48 (Mumme *et al.* (2013), highlighting the constraints of local conditions on compositional variation in a single deposit. All studies of the homologue N=2 from Boliden, including the present data, affirm these are Se-rich specimens (~3-4 wt.%; Tables 2 and S3). The izoklakeite reported here from Boliden is also Se-rich (~5 wt.%; Table 1). The Se-rich environment from which these sulphosalts have formed is further emphasised by the presence of 2.81 wt% Se in Bi-rich jamesonite (Table S4). Selenium-bearing assemblages of jamesonite and tintinaite are also reported from Úhorná (Spišsko Gemerské Rudohorie Mts., Slovakia; Pršek and Peterek, 2008). The Korunka Mine specimen used for refinement of kobellite crystal structure (Miehe, 1971) is from the same sulphosalt rich, hydrothermal vein system (~1200 veins) in Eastern Slovakia as the Úhorná specimen. As at Boliden, we note that the Tti:Kbl ratio changes from 60:40 to 44:56, emphasizing the presence of both tintinaite and kobellite in the same orefield.

Mirroring the Boliden kobellite homologues, distinct ranges of composition for the same sulphosalt within a given district or province are also reported (Moëlo *et al.*, 1995). At Boliden, co-crystallisation of the two sulphosalts is reflected by local variations in the Sb:Bi ratios in tintinaite throughout the three analysed areas in sample 1061a, i.e., the lowest ratio of 66:36 in area 2 when co-existing with izoklakeite, and highest (69:31) when co-existing with jamesonite in area 3 (Table 2).

Figure 14 compares the compositional data for the Boliden specimens (Tables 1-3) with published data from other localities and ideal end members for the two series (Table S3 Supplementary Materials, and references therein). The relative proportions of Pb, Bi and Sb, the three main elements in the M sites defining the structural modules for the two homologues, are depicted on the plot of  $Pb^*/(Pb^*+Bi+Sb-Ag)$  versus  $Bi/(Sb+Bi)$  where  $Pb^*=(Pb+Ag+Cd+Zn)$  in Figure 14.

Izoklakeite data separates into two groups: (i) “Bi-rich izoklakeite” encompassing the specimen from Zervreila Lake, Switzerland (Armbruster and Hummel, 1987) and material from Guitashan, China (Li *et al.*, 2019), and (ii) izoklakeite from the type locality (Harris *et al.*, 1986), Vena, Sweden (Zakrzewski and Makovicky, 1986) and the specimens from Boliden reported here. In addition to these, specimens from France and Portugal (Moëlo *et al.*, 1995) are defined from chemistry alone. Among these, Bazoges (France) includes both types of izoklakeite. Notably, Boliden izoklakeite plots at the lower end of the  $Bi/(Sb+Bi)$  range and within the central part ( $x=1$ ) of the N=4 homologue band.

Higher-Bi specimens of homologue N=2, kobellite *sensu stricto*, forms a tight cluster with  $0.55 > Bi/(Sb+Bi) > 0.7$  including data from Korunka Mine (Miehe, 1971), Guitashan (Li *et al.*, 2019), Hvena (Sweden), Raleigh (USA) (Moëlo *et al.*, 1984), Les Chalanches (France) and Pedra Luz (Portugal) (Moëlo *et al.*, 1995). Two of the Boliden specimens around  $Bi/(Sb+Bi)=0.5$  (Moëlo *et al.*, 1984; Mumme *et al.*, 2013) lie at the boundary between kobellite and tintinaite. The other tintinaite

data include specimens from Rossland (Canada; Moëlo *et al.*, 1984), Pedra Luz (Moëlo *et al.*, 1995), Uhorna (Slovakia; Pršek and Peterek, 2008), data from Boliden (Wagner and Jonsson, 2001, and the present work, and the Sb-pure tintinaite from Tintina (Harris *et al.*, 1986; Moëlo *et al.*, 1984). The tintinaite-kobellite data plots along the middle to upper part of N=2 band, with Korunka Mine kobellite at x=0.

#### *Primary nanoscale intergrowths: jigsaw patterns evolving from chessboard structures*

Widespread nanoscale intergrowths between tintinaite and izoklakeite (Figs. 3, 10-12) account for compositional fields in terms of  $M^{2+}(+Ag^{1+})$  and  $M^{3+}$  cations when analysed at the micron-scale (Fig. 3). It is however interesting to note that the range of N values, 2.01-2.08 for tintinaite (Tables 2, 3) are slightly in excess of ideal N=2, whereas the range of N values for izoklakeite, 3.76-3.94 (Table 1) are in deficit relative to ideal N=4. This mirrors results for N values of kobellite homologues elsewhere (Table 4). Challenges in calculation of N values from EPMA data are introduced by excess of Cu over the 2 a.p.f.u. in the tetrahedral site. In addition to Pb and (Sb,Bi) correction due to Ag incorporation (see above), attributing excess Cu to either Pb or (Sb,Bi) sites drives significant changes of N (Table 4; Fig. 14), as observed for kobellite from Raleigh (Moëlo *et al.*, 1984) and kobellite and izoklakeite from Les Chalanches (Moëlo *et al.*, 1984; 1995). The Bi-rich izoklakeite from Zervreila Lake (Armbruster and Hummel, 1987) gives N=4.08 and 4.54, if Ag is incorporated within the (Sb,Bi) or Pb sites, respectively. The N excess of tintinaite, and N deficit of izoklakeite, may indicate that, at the scale of the electron probe spot, the analyzed volume of each sulfosalt integrates a minor fraction of the other sulfosalt as a syntactic intergrowth.

Difficulties in attributing specific schemes of (Sb,Bi,Pb) ordering in izoklakeite that markedly differ in chemistry were discussed in detail by Armbruster and Hummel (1987) using the examples of Bi- and Sb-rich varieties from Lake Zervreila and Vena (Makovicky and Mumme, 1986). Although this does not affect the identification of building modules by HAADF STEM imaging of either Bi- or Sb-rich izoklakeite and kobellite and tintinaite, as shown for specimens from Gutaishan (Iz<sub>35</sub> and Kbl<sub>61</sub>; Li *et al.*, 2019) and Boliden (Iz<sub>60</sub> and Tti<sub>60</sub>; Figs. 6, 7), it is nevertheless reflected in the atom-resolution mapping of izoklakeite and tintinaite (Fig. 8).

A novel feature of the sulphosalt intergrowths from Boliden are the SnS and PbS modules with n=12 and 24, respectively, imaged as arrays of combined SnS and PbS modules in either izoklakeite or tintinaite (Fig. 12). These correspond to modules suggested for a hypothetical N=3 member of the kobellite series (Makovicky and Mumme, 1986) with an estimated structural formula (without Ag) that can be given as:  $(Cu_{2-x}Fe_x)Pb_{18+x}(Sb,Bi)_{18-x}S_{46}$ . The structure of the N=3 homologue is illustrated as Figure 15.

Structural versatility of these sulphosalts is moreover reflected in the ability to combine modules corresponding to different homologues such as  $\text{SnS}_{\text{Ti}=\text{Kbl}}$  and  $\text{PbS}_{\text{N}=3}$ . Other structures can be derived forming a broader family of Pb-Bi-Sb sulphosalts considered as kobellite homeotypes (Makovicky and Balić-Žunić, 2023, and references therein).

Structural arrangements in kobellite homologues have been described as ‘cyclically twinned’ (Makovicky, 1985), ‘boxwork’ (Makovicky, 1997), ‘chessboard’ (Li *et al.*, 2019) or quasi-chessboard (Makovicky and Balić-Žunić, 2023). Chessboard structures are highly adaptable to accommodating nanoscale intergrowths between modules of variable sizes and combinations of thereof (Figs. 11, 12), leading to smallest scale 2D jigsaw-like patterns.

Such physical-chemical behaviour can be considered as a type of microstructural evolution in complex nonlinear systems, a topic of interest from both theoretical and engineering viewpoints. For instance, quasiperiodic two-phase nanowire chessboard structures are common in a variety of materials from decomposing alloys to oxide ceramics and have been modelled as tweed structures with an underlying chessboard feature evolving during pseudospinodal decomposition (Ni and Khachatryan, 2009). Chessboard-like supramolecular structures on  $\text{Au}_{(111)}$  surfaces designed for chemical functionalization of bio-sensors and molecular electronics (Dou *et al.*, 2015), or broadband chessboard surfaces with double-layer for electromagnetic gap band (Mighani and Dadashzadeh, 2016), are among materials with block modularity akin to those discussed here.

#### *Lone electron pair micelles- depicting Sb-rich kobellite homologues*

The wide variety of distorted polyhedra, ranging from six to nine-fold coordination environments, is the basis for crystal structural modularity shared by Pb-Bi-Sb-sulphosalts (Makovicky, 1997, and references therein). This is due to variable stereochemical activity of the lone electron pair of  $\text{Pb}^{2+}$ ,  $\text{Bi}^{3+}$  and  $\text{Sb}^{3+}$  which, statistically, has a decreasing influence on distortion of the coordination polyhedra with increasing atom size  $\text{Sb} < \text{Bi} < \text{Pb}$  (Armbruster and Hummel, 1987). Makovicky and Mumme (1986) discussed the formation of lone electron pairs micelles as a means to structurally accommodate stereochemical active pairs along interfaces in sulphosalts with reference to kobellite homologues. These concepts were subsequently taken to defining modularity in Pb-Sb-sulphosalts based on the arrangement of micelles into ‘fish-bone’ zigzag layers (e.g., Moëlo *et al.*, 2000; Biagioni *et al.*, 2016).

An outstanding result of the present study is depiction of the dark line patterning through the middle of  $\text{SnS}$  modules on the HAADF STEM images of Sb-rich homologues (Figs. 6, 7). These are directly attributable to the lone electron pair micelles in the structures, as outlined for example in izoklakeite (Makovicky and Mumme, 1986). Notably, these features were not identified on the HAADF STEM images of Bi-rich kobellite homologues from Gutaishan (Li *et al.*, 2019), and thus

confirm the stronger influence of Sb relative to Bi atoms in terms of stereochemical activity of the lone electron pair (Armbruster and Hummel, 1987).

Ultralow thermal conductivity is a material property linked to the effect of lone electron pair micelles in strengthening bond anharmonicity as assessed in a synthetic  $\text{MnPb}_{16}\text{Sb}_{14}\text{S}_{38}$  sulphosalt (Dawahre *et al.*, 2020). This study acknowledged the lack of thermal transport behaviour studies of Pb-Sb-sulphosalts despite their significant potential in terms of technological applications, ranging from thermoelectric energy conversion to thermal barrier coatings (e.g., Dittrich *et al.*, 2009).

### *Secondary textures; a record of metamorphic deformation*

The range of shear, twist, jogs, and displacement textures occurring as defects, crosscutting veinlets no more than a few nm wide, or along crystallographic planes in kobellite homologues (Figs. 10g, h and 13) are secondary features attributable to superimposed syn-metamorphic deformation. These are associated with the redistribution of Bi and Se (Fig. 13f) and led to late formation of the Bi chalcogenides identified in areas of the samples bearing evidence of trace element remobilisation at the micron-scale (Fig. 2).

Such interpretations are concordant with assertions that sulphosalt-rich vein ores (containing kobellite homologues) experienced extensive ductile deformation post-dated by decomposition textures leading to formation of Se-rich assemblages (including laitakarite) at Boliden (Wagner and Jonsson, 2001). The twists, shears and displacements of building modules or the low-angle imbrication boundaries in kobellite homologues resemble chain-width disorder in non-conventional pyriboles produced during syn-tectonic events (e.g., Konishi *et al.*, 2010; Campo-Rodriguez *et al.*, 2024, in press). Twists and shears recorded by pyrite during brittle to ductile transition are among nanoscale textures associated with Au and accompanying trace element (re)mobilisation in brecciated ores (Ehrig *et al.*, 2023).

## **Summary and Implications**

The findings of the present study are summarised below.

- (1) Sulphosalt assemblages from Boliden (Sweden) comprise micron- to nanoscale intergrowths of Se-rich izoklakeite ( $\text{Iz}_{60}\text{Gie}_{40}$ ) and tintinaite ( $\text{Tti}_{66}\text{Kbl}_{34}$ ) with average formulae and calculated homologue number (N) given as:  
 $(\text{Cu}_{1.88}\text{Fe}_{0.18})_{2.06}(\text{Pb}_{22.92}\text{Ag}_{1.47}\text{Cd}_{0.01}\text{Zn}_{0.01})_{24.41}(\text{Sb}_{13.12}\text{Bi}_{8.69})_{21.8}(\text{S}_{50.19}\text{Se}_{6.43}\text{Te}_{0.12})_{56.73}$ ,  $N=3.83$ ,  
and  $(\text{Cu}_{1.31}\text{Fe}_{0.74})_{2.05}(\text{Pb}_{10.58}\text{Ag}_{0.18}\text{Cd}_{0.05}\text{Zn}_{0.02})_{10.83}(\text{Sb}_{10.2}\text{Bi}_{5.23})_{15.43}(\text{S}_{32.22}\text{Se}_{2.46})_{34.7}$  and  
calculated  $N=2.05$ , respectively. The two sulphosalts are also Se-rich, 4.83 wt.% and 3.3 wt.%, for izoklakeite and tintinaite.

- (2) HAADF STEM imaging reveals chessboard structures comprising PbS and SnS building modules with the number of atoms (bright dots on images) in the octahedral (M) sites counted as:  $n_1=18$  and  $n_2=8$  for tintinaite, and  $n_1=30$  and  $n_2=16$  for izoklakeite. The homologue number can be calculated using the formula:  $N=(n_1/6)-1$  and  $N=n_2/4$  for PbS and SnS modules giving  $N_{Ti}=2$  and  $N_{Lz}=4$ .
- (3) A new homologue, defined by  $n=12$  and  $24$  for SnS and PbS modules, corresponding to the  $N=3$  member of the kobellite series is identified as single or double units within areas with intergrowths between tintinaite and izoklakeite.
- (4) HAADF STEM imaging of Sb-rich kobellite homologues reveals features attributable to lone electron pair micelles.
- (5) The first atomic-resolution chemical mapping of Pb-Bi-Sb-sulphosalts shows a correlation with crystal structural modularity. The EDS STEM maps also highlight sites in the SnS modules of tintinaite in which  $Sb>Bi$ . Although this is only a qualitative assessment, the data is concordant with the overall Sb-rich composition of the Boliden specimen.
- (6) Widespread coherent nanoscale intergrowths between kobellite homologues define jigsaw patterns evolving from chessboard structures and are considered to have formed during co-crystallisation of the two phases.
- (7) A range of displacement textures and crosscutting veinlets (a few nm in width) are interpreted as evidence for superimposed syn-metamorphic deformation and are associated with the redistribution of Bi and Se.

Whereas crystal-structural modularity in Pb-Bi-sulphosalts is readily predictable from principles established some decades ago (Makovicky, 1997, and references therein), imaging and mapping using HAADF STEM techniques is a novel and ideally suited way to characterise such phases and their relationships down to the nanoscale (Ciobanu *et al.*, 2016). These tools hold untapped potential to unravel intricate pattern evolution of chessboard structures with applications across mineralogy but extending into allied fields of materials science and nanotechnology.

**Acknowledgements.** This work was funded by The University of Adelaide through a “Women’s Research Excellence Award” to C.L.C. and seed funding for nanoscale studies from BHP Olympic Dam. We appreciate the valuable comments and insights from Yves Moëlo, including his suggestion to include Figure 15. We thank Stuart Mills for his editorial handling of the manuscript.

**Competing interests.** There are no conflicts of interest to declare.

**Supplementary Materials:** Tables S1-S4, Figures S1-S3

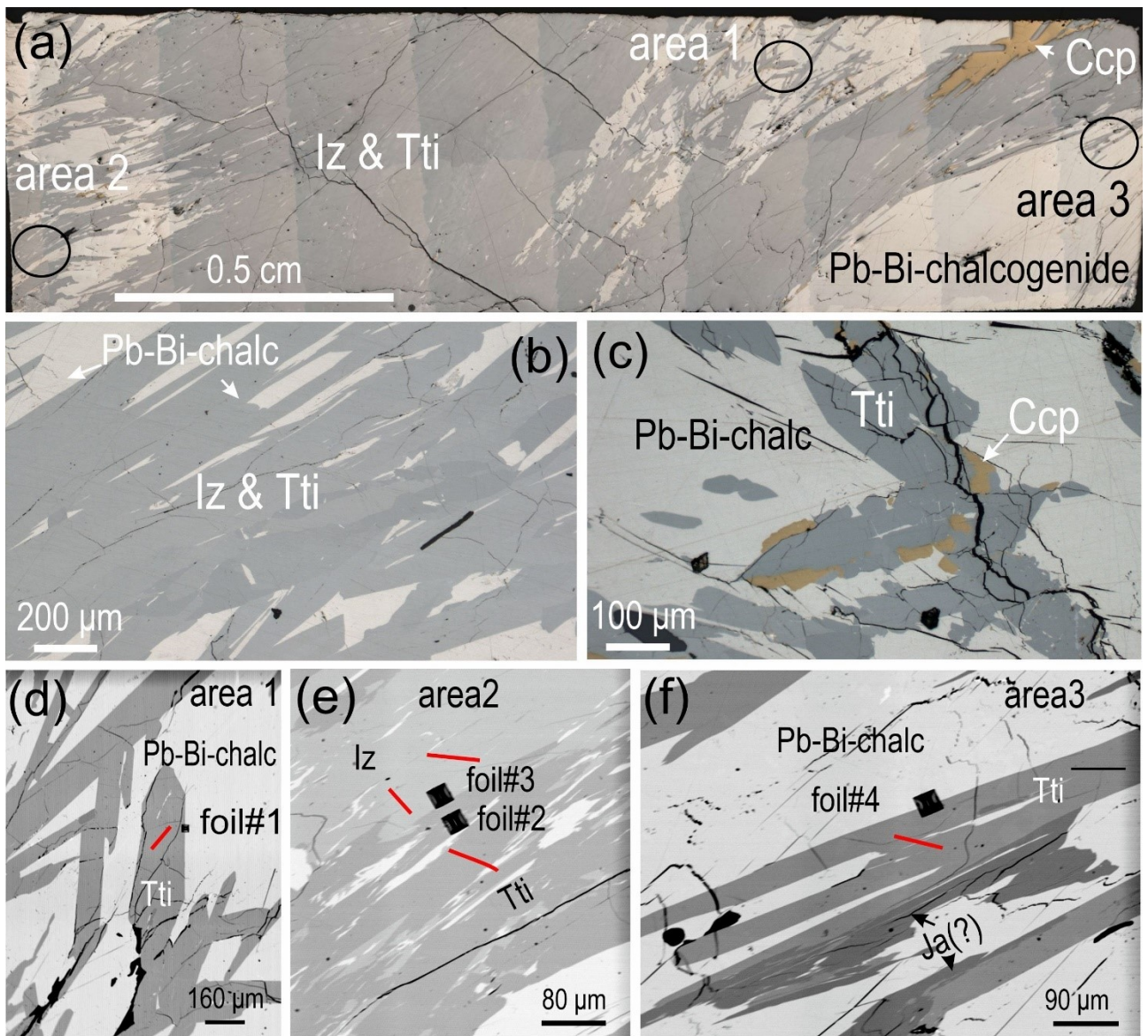
## References

- Armbruster T. and Hummel W. (1987) (Sb,Bi,Pb) ordering in sulfosalts: Crystal-structure refinement of a Bi-rich izoklakeite *American Mineralogist*, **72** 821-831.
- Biagioni C., Mořlo Y., Orlandi P. and Stanley C.J. (2016) Lead-antimony sulfosalts from Tuscany (Italy). XVII. Meerschautite,  $(\text{Ag,Cu})_{5.5}\text{Pb}_{42.4}(\text{Sb,As})_{45.1}\text{S}_{112}\text{O}_{0.8}$ , a new expanded derivative of owyheeite from the Pollone mine, Valdicastello Carducci: occurrence and crystal structure. *Mineralogical Magazine*, **80**, 675–690
- Campo-Rodriguez Y.T., Ciobanu C.L., Slattery A., Cook N.J., Schutesky M.E., Ehrig K., King S.A. and Yao J. (2024, in press) Polysomatic intergrowths between amphiboles and non-classical pyriboles in magnetite: smallest-scale features recording a protracted geological history. *American Mineralogist*; <https://doi.org/10.2138/am-2023-9188>
- Ciobanu C.L., Cook N.J., Pring A. and Green L. (2011) Focussed ion beam - transmission electron microscopy applications in ore mineralogy: bridging micron- and nanoscale observations. *Ore Geology Reviews*, **42**, 6–31.
- Ciobanu C.L., Cook N.J., Maunders C., Wade B.P. and Ehrig K. (2016) Focused Ion Beam and Advanced Electron Microscopy for Minerals: Insights and Outlook from Bismuth Sulphosalts. *Minerals*, **6**, 112.
- Dawahre L., Lu R., Djieutedjeu H., Lopez J., Bailey T.P., Buchanan B., Yin Z., Uher C. and Poudeu P.F.P. (2020) Lone-Electron-Pair Micelles Strengthen Bond Anharmonicity in  $\text{MnPb}_{16}\text{Sb}_{14}\text{S}_{38}$  Complex Sulfosalt Leading to Ultralow Thermal Conductivity. *ACS Applied Materials and Interfaces*, **12**, 44991–44997.
- Dittrich H., Stadler A., Topa D., Schimper H.-J. and Basch A. (2009) Progress in sulfosalt research. *Physica status solidi*, **206**, 1034–1041.
- Dou R., Yang Y., Zhang P., Zhong D., Fuchs H., Wang Y. and Lifeng Chi (2015) Building chessboard-like supramolecular structures on Au(111) surfaces. *Nanotechnology*, **26**, 385601.
- Ehrig K., Ciobanu C.L., Verdugo-Ihl M.R., Dmitrijeva M., Cook N.J. and Slattery A. (2023) Lifting the cloak of invisibility: Gold in pyrite from the Olympic Dam Cu-U-Au-Ag deposit, South Australia. *American Mineralogist*, **108**, 259-276.
- Graeser S. and Harris D.D. (1986) Giessenite from Giessen near Binn, Switzerland: New data. *The Canadian Mineralogist*, **24**, 19-20.
- Grip E. and Wirstam Å. (1970) The Boliden sulphide deposit. A review of geo-investigations carried out during the lifetime of the Boliden mine, Sweden (1924–1967). *Sveriges Geologiska Undersökning*, **C651**.
- Harris D.C., Jambor J.L., Lachance G.R. and Thorpe R.I. (1968) Tintinaite, the antimony analogue of kobellite. *The Canadian Mineralogist*, **9**, 371-382.
- Harris D.C., Roberts A.C., and Criddle A.J. (1986) Izoklakeite, a new mineral species from Izok Lake, Northwest Territories. *The Canadian Mineralogist* **24**, 1-5.
- Konishi H., Xu H., and Dymek R.F. (2010) High-resolution TEM study of jimthompsonite, chesterite, and chain-width disorder in Archean ultramafic rocks from Isua, West Greenland. *American Mineralogist*, **95**, 73–80.
- Li W., Ciobanu C.L., Slattery A., Cook N.J., Liu W., Wade B.P. and Xie G.Q. (2019) Chessboard structures: Atom-scale imaging of homologs from the kobellite series. *American Mineralogist*, **104**, 459–462.

- Makovicky E. (1985) Cyclically twinned sulphosalt structures and their approximate analogues. *Zeitschrift für Kristallographie* **173**, 1- 23.
- Makovicky E. (1997) Modular crystal chemistry of sulphosalts and other complex sulphides. In *Modular Aspects of Minerals* (S. Merlino, ed.). *European Mineralogical Union, Notes in Mineralogy* **1**, 237-271.
- Makovicky E. and Balić-Žunić T. (2023) On the homeotypes of kobellite. *Mineralogy and Petrology*, **117**, 209–217.
- Makovicky E. and Karup-Møller S. (1986) New data on giessenite from the Bjørkåsen sulfide deposit at Otofthen, northern Norway. *The Canadian Mineralogist*, **24**, 21-25.
- Makovicky E. and Mumme W.G. (1986) The crystal structure of izoklakeite,  $Pb_{51.3}Sb_{20.4}Bi_{19.5}Ag_{1.2}Cu_{2.9}Fe_{0.7}S_{114}$ . The kobellite homologous series and its derivatives *Neues Jahrbuch für Mineralogie, Abhandlungen*, **153**, 121-145.
- Makovicky E. and Nørrestam R. (1985) The crystal structure of jaskolskiite,  $Cu_xPb_{2+x}(Sb,Bi)_{2-x}S_5$  ( $x \sim 0.2$ ), a member of the meneghinite homologous series. *Zeitschrift für Kristallographie*, **171**, 179-194.
- Miehe G. (1971) Crystal structure of kobellite. *Nature Physical Science*, **231**, 133-134.
- Mighani M. and Dadashzadeh G. (2016) Broadband RCS reduction using a novel double layer chessboard AMC surface. *Electronics Letters*, **52**, 1253–1255.
- Moëlo Y., Jambor J.L. and Harris D.C. (1984) Tintinaïte et sulfosels associés de Tintina (Yukon): Tintinaïte et sulfosels associés de Tintina (Yukon): la cristallographie de la série de la kobellite. *The Canadian Mineralogist*, **22**, 219-226.
- Moëlo Y., Roger D., Maurel-Palacin D., Marcoux E. and Laroussi A. (1995) Chemistry of some Pb-(Cu, Fe)-(Sb, Bi) sulfosalts from France and Portugal. Implications for the crystal chemistry of lead sulfosalts in the Cu-poor part of the  $Pb_2S_2-Cu_2S-Sb_2S_3-Bi_2S_3$  System. *Mineralogy and Petrology*, **53**, 229-250.
- Moëlo Y., Meerschaut A. Orlandi P. and Palvadeau P. (2000) Lead-antimony sulfosalts from Tuscany (Italy): II - Crystal structure of scainiite,  $Pb_{14}Sb_{30}S_{54}O_5$ , an expanded monoclinic derivative of  $Ba_{12}Bi_{24}S_{48}$  hexagonal sub-type (zinkenite group). *European Journal of Mineralogy* **12**, 835-846.
- Moëlo Y., Makovicky E., Mozgova N.N., Jambor J.L., Cook N., Pring A., Paar W., Nickel E.H., Graeser S., Karup-Møller S., Balić-Žunić T., Mumme W.G., Vurro F., Topa D., Bindi L., Bente K. and Shimizu M. (2008) Sulfosalt systematics: a review. Report of the sulfosalt sub-committee of the IMA Commission on Ore Mineralogy. *European Journal of Mineralogy*, **20**, 7-46.
- Mumme W.G., Gable R.W. and Wilson N. (2013) A crystal structure determination of (selenian) kobellite from the Boliden Mine, Sweden. *Neues Jahrbuch für Mineralogie, Abhandlungen*, **191**, 109-115.
- Ni Y. and Khachatryan A.G. (2009) From chessboard tweed to chessboard nanowire structure during pseudospinodal decomposition. *Nature Materials*, **8**, 410-414.
- Niizeki N. and Buerger MJ (1957) The crystal structure of jamesonite,  $FePb_4Sb_6S_{14}$ . *Zeitschrift für Kristallographie* **109** 161-183.
- Nuffield E.W. (1948). Observations on kobellite. *University of Toronto Studies: VI. Geological Series*, **52**, 86-89.

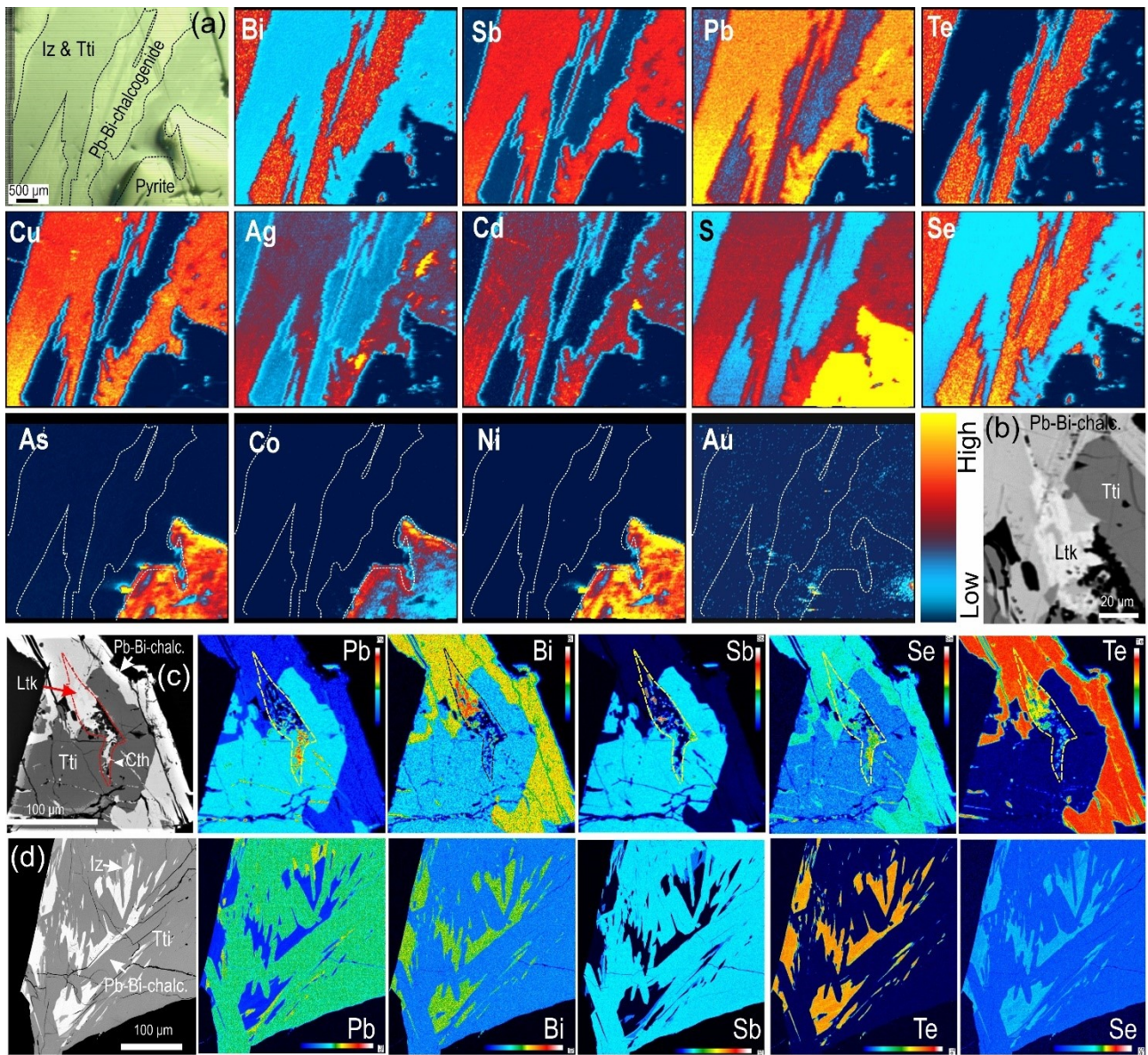
- Ödman O. (1941) Geology and ores of the Boliden deposit, Sweden. *Sveriges Geologiska Undersökning*, **C438**.
- Pršek J. and Peterek D. (2008) Bi-Se-Te mineralization from Úhorná (Spišsko Gemerské Rudohorie Mts., Slovakia): A preliminary report. *Mineralogia*, **39**, 87–103.
- Wagner T. and Jonsson E. (2001) Mineralogy of sulfosalt-rich vein-type ores, Boliden massive sulfide deposit, Skellefte district, northern Sweden. *The Canadian Mineralogist*, **39**, 855-872.
- Wagner T., Klemm R., Wenzel T. and Mattsson B. (2007) Gold upgrading in metamorphosed massive sulfide ore deposits: Direct evidence from laser-ablation–inductively coupled plasma–mass spectrometry analysis of invisible gold. *Geology*, **35**, 775-778.
- Weihed J.B., Bergström U., Billström K. and Weihed P. (1996) Geology, tectonic setting, and origin of the Paleoproterozoic Boliden Au-Cu-As deposit, Skellefte district, northern Sweden. *Economic Geology*, **91**, 1073-1097.
- Zakrzewski M.A. (1984) Jaskólskiite, a new Pb-Cu-Sb-Bi sulfosalt from the Vena Deposit, Sweden. *The Canadian Mineralogist*, **22**, 481-485.
- Zakrzewski M.A. and Makovicky E. (1986) Izoklakeite from Vena, Sweden, and the kobellite homologous series. *The Canadian Mineralogist*, **24**, 7-18.

## Figure captions



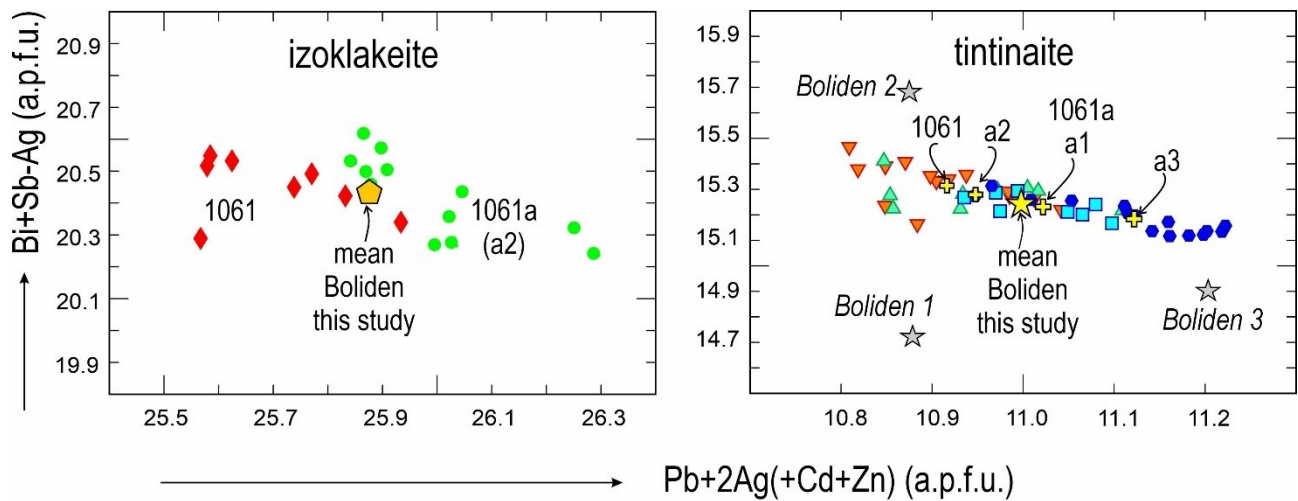
Ciobanu et al. Figure 1

**Figure 1.** Reflected light microphotographs (a-c) and back scattered electron (BSE) microscopy images (d-f) showing micron-scale intergrowths between tintinaite (Tti), izoklakeite (Iz) and Pb-Bi-chalcogenides (Pb-Bi-chalc) in sample/polished block 1061a. Note minor chalcopyrite (Ccp) is also present. Areas studied at the nanoscale are marked on the overall map of the sample (a). (d-f) Detailed images of areas 1-3 showing the stamps of FIB cuts from which the analysed S/TEM foils were prepared as well as the profiles for EMPA spot analyses (red lines). Tti–tintinaite.



Ciobanu et al. Figure 2

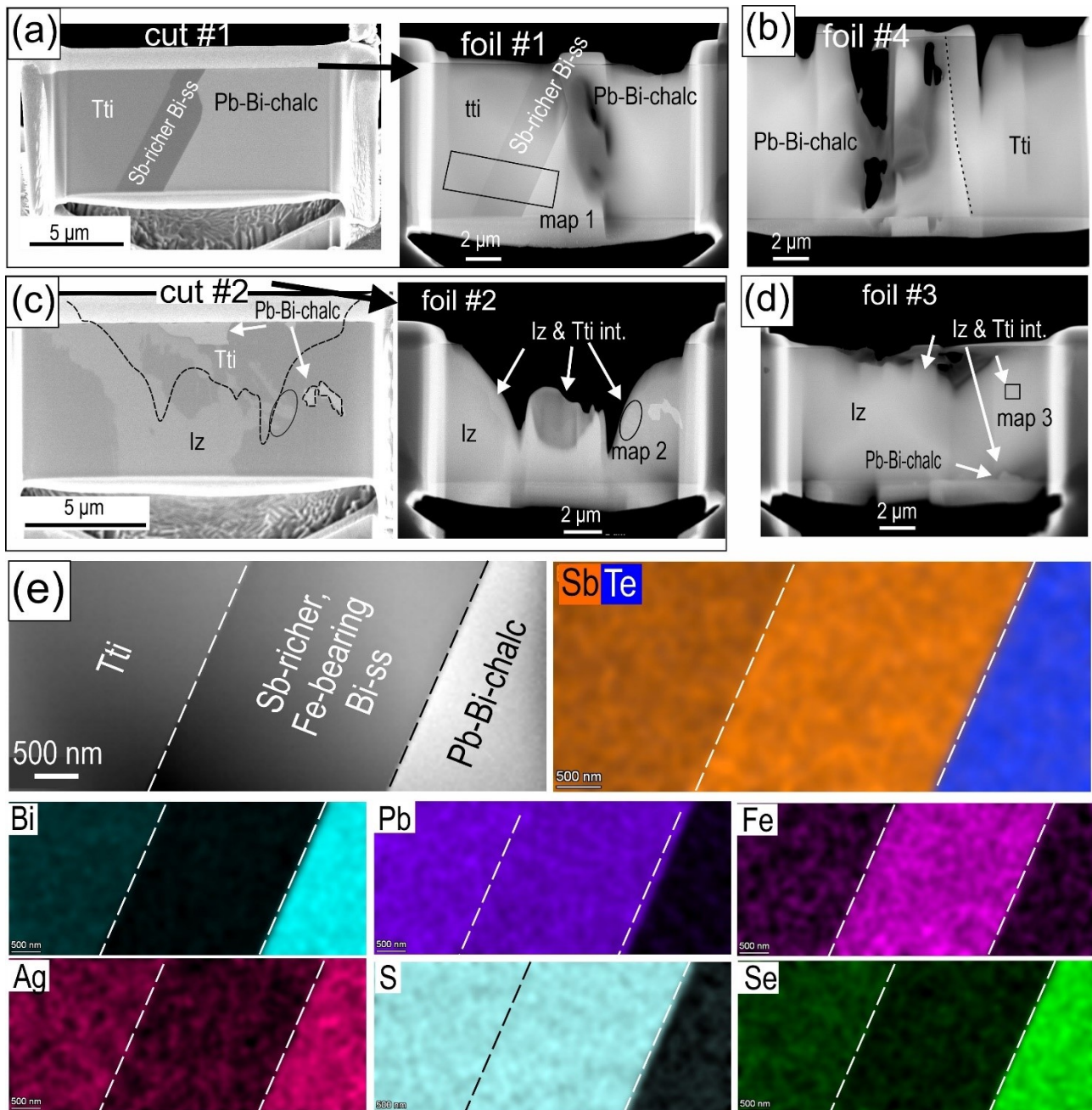
**Figure 2.** (a) LA-ICPMS element maps, (b) BSE image, and (c, d) EPMA element maps showing micron-scale distribution of main and minor/trace elements within intergrowths of tintinaite (Tti), izoklakeite (Iz) and Pb-Bi-chalcogenides (sample 1061). Note that Se is richest in the Pb-Bi-chalcogenide in (a, c, d). Silver is higher in the sulphosalt intergrowths whereas Au occurs as minute inclusions (high intensity spots) more abundant across a transect from pyrite into the Bi-mineral intergrowths in (a). (b) Inclusion of laitakarite (Ltk;  $\text{Bi}_4\text{Se}_3$ ) at the junction between lamellae of Pb-Bi-chalcogenide and tintinaite. (c) Contact between tintinaite and Pb-Bi-chalcogenide is marked by fractures crosscutting the sulphosalt. These are shown by relative depletion in Pb, Bi, and Sb and enrichment in Se. Such areas of element redistribution are accompanied by formation of laitakarite and clausthalite (Cth) marked by red outline. (d) Tintinaite with interstitial Pb-Bi-chalcogenide. Note small area of izoklakeite with the highest Pb concentration.



Ciobanu et al. Figure 3

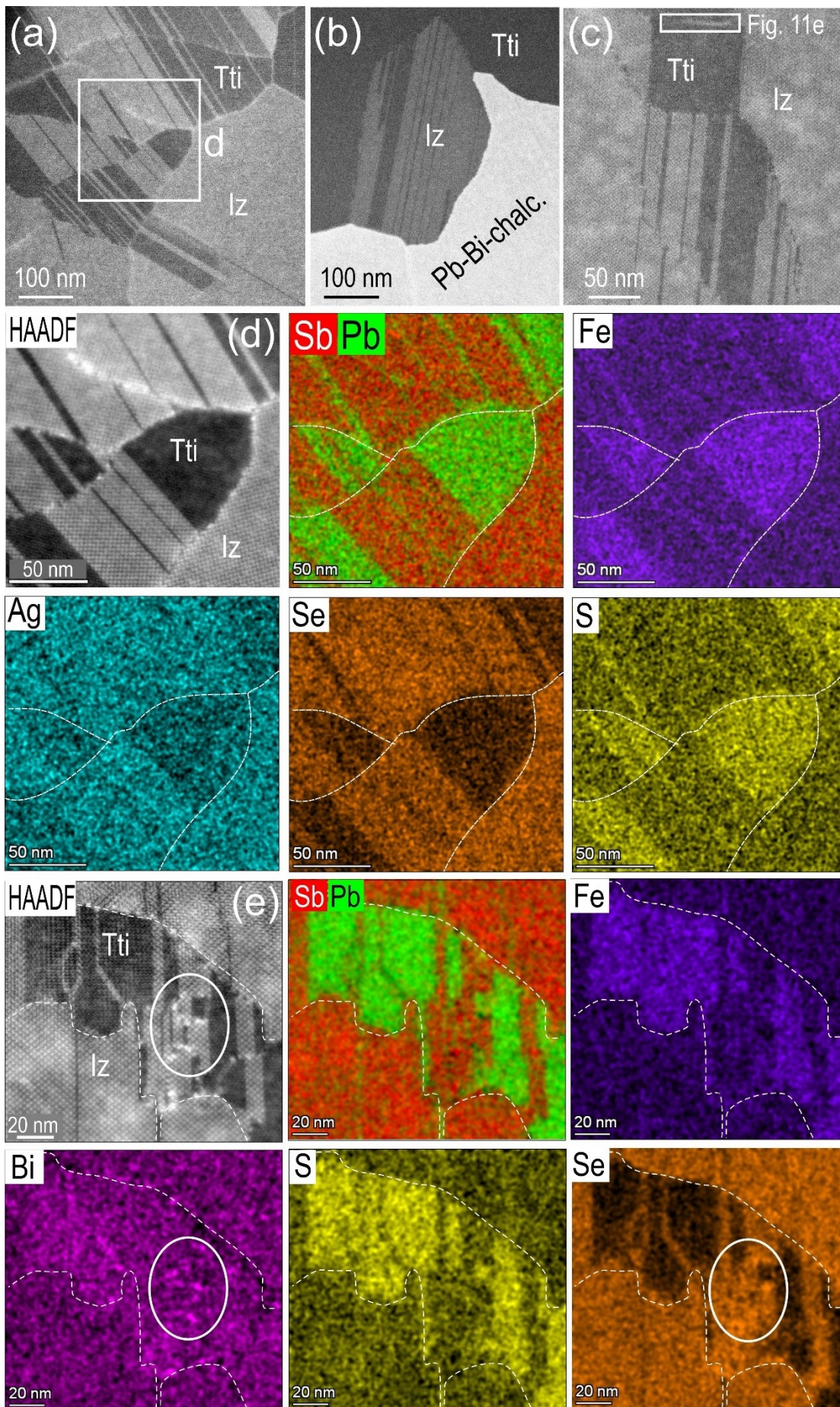
**Figure 3.** Binary plots of Bi+Sb-Ag vs. Pb+2Ag+Cd+Zn (a.p.f.u.) showing subtle differences in chemistry of izoklakeite and tintinaite between the two analysed samples (as labelled). Data from Tables 1-3 and Tables S1-3 Supplementary Material. For comparison, data for kobellite-tintinaite from Moëlo *et al.* (1984), Mumme *et al.* (2008) and Wagner and Jonsson (2001) are plotted and labelled as *Bol1*, *Bol2*, and *Bol3*, respectively.

Prepublished Article



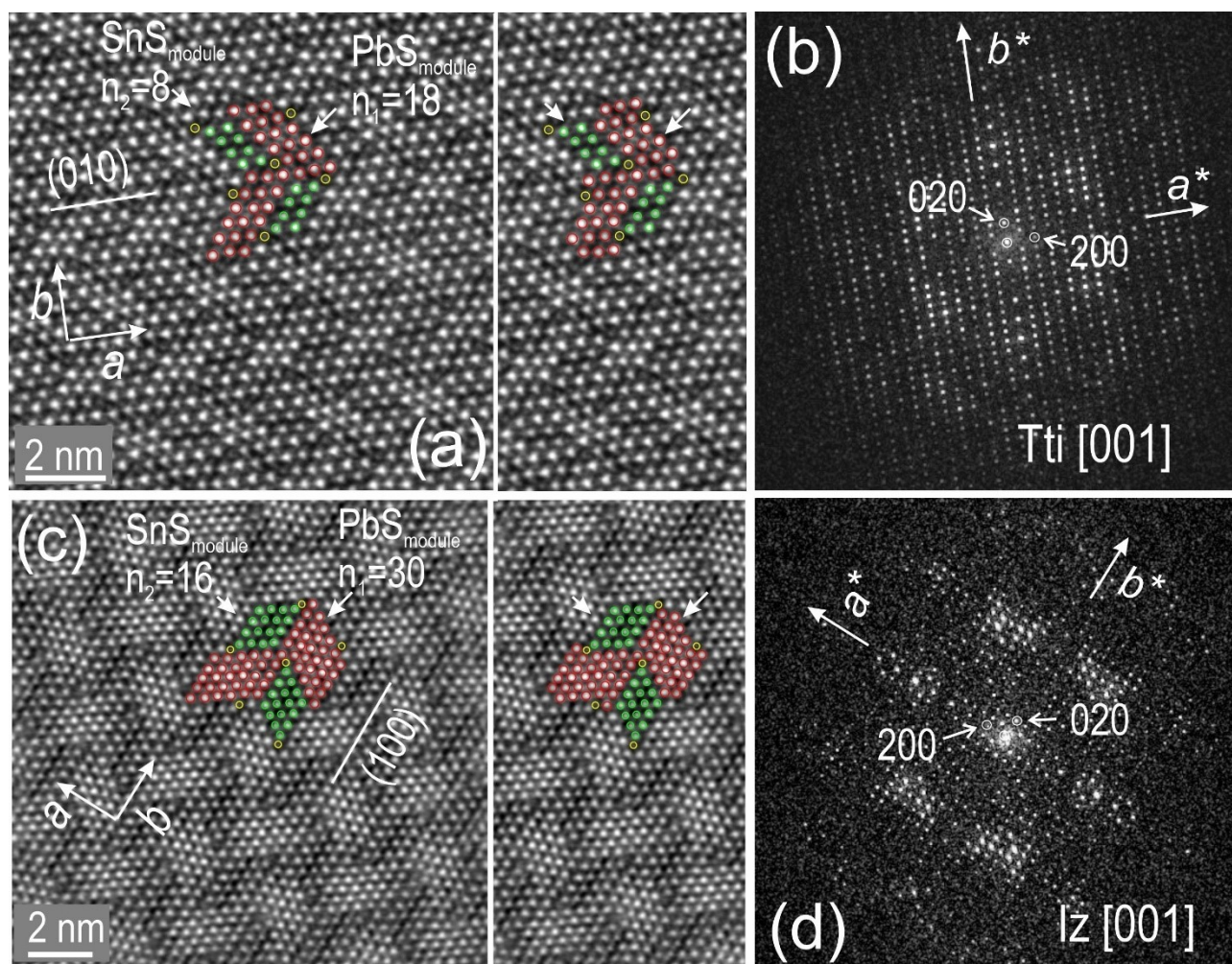
Ciobanu et al. Figure 4

**Figure 4.** (a-d) Images showing the four foils as labelled which have targeted contacts between the three components in the lamellar intergrowths, tintinaite (Tti), izoklakeite (Iz) and Pb-Bi-chalcogenide. Foils #1 and #2 are shown both before (left) and after (right) thinning. (e) HAADF STEM image and EDS STEM element maps of the grain boundary between tintinaite and Pb-Bi-chalcogenide (marked by rectangle map 1 in (a)) showing the presence of a Sb-rich bismuth sulphosalt lamella between the two phases. Note the relative depletion in Bi, Ag and Se, and the marked Fe enrichment of this lamella relative to tintinaite. The contacts between tintinaite and izoklakeite in foils #3 and #4 are marked by the presence of small Pb-Bi-chalcogenide inclusions.



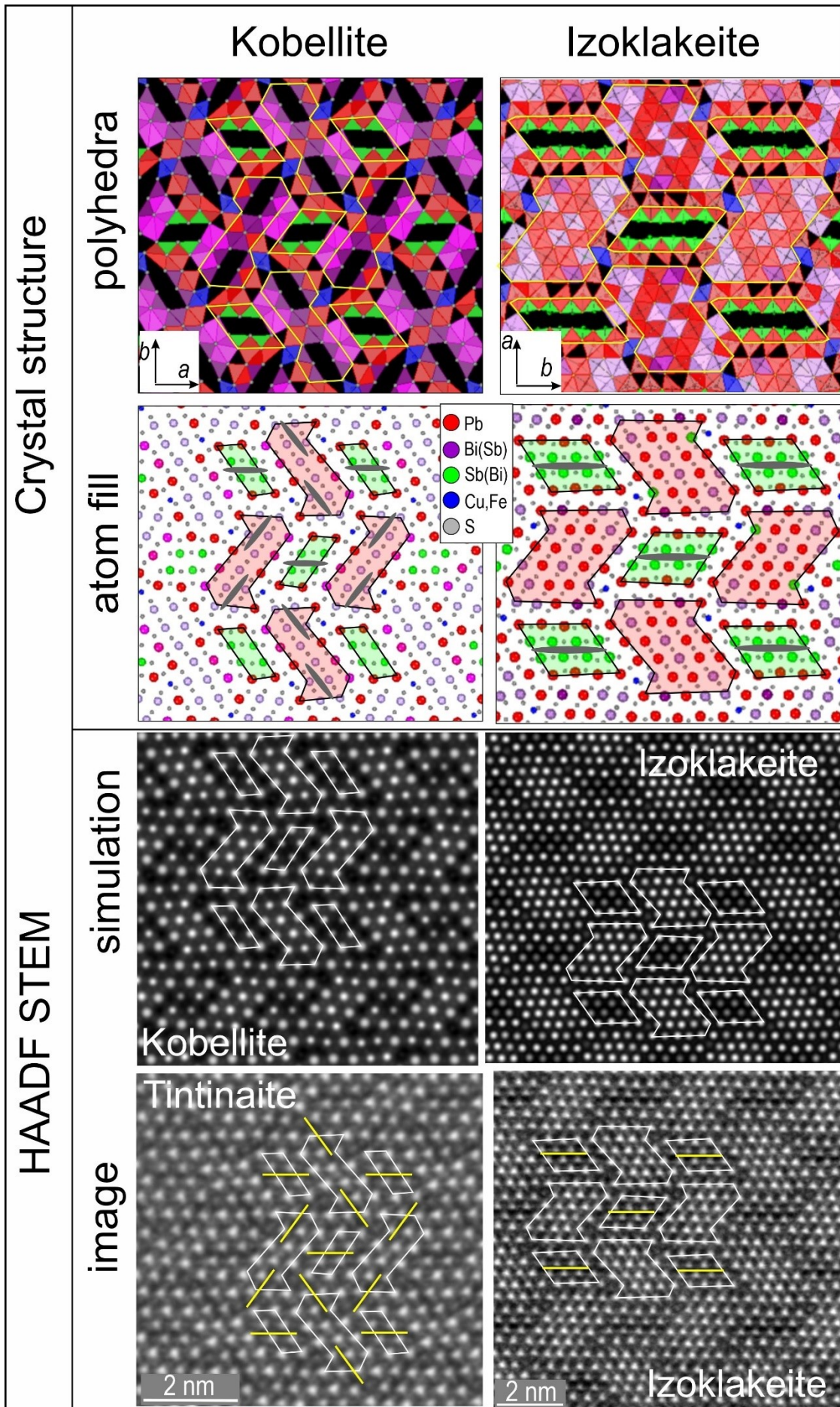
Ciobanu et al. Figure 5

**Figure 5.** Intergrowths between tintinaite (Tti), izoklakeite (Iz) and Pb-Bi-chalcogenide as HAADF STEM images (a-c) and EDS STEM maps 2 and 3 (d, e) marked on Figure 4c and d. The mapped areas are marked by the rectangles as labelled. Note that contacts display smaller grains with fine, nanometre-scale lamellar intergrowths between the two sulphosalts. (d) (e) Maps showing the relative increase in Pb, Fe and S and decrease in Se between tintinaite and izoklakeite. Remobilisation of Se (circled area) along the contacts between the finest intergrowths.



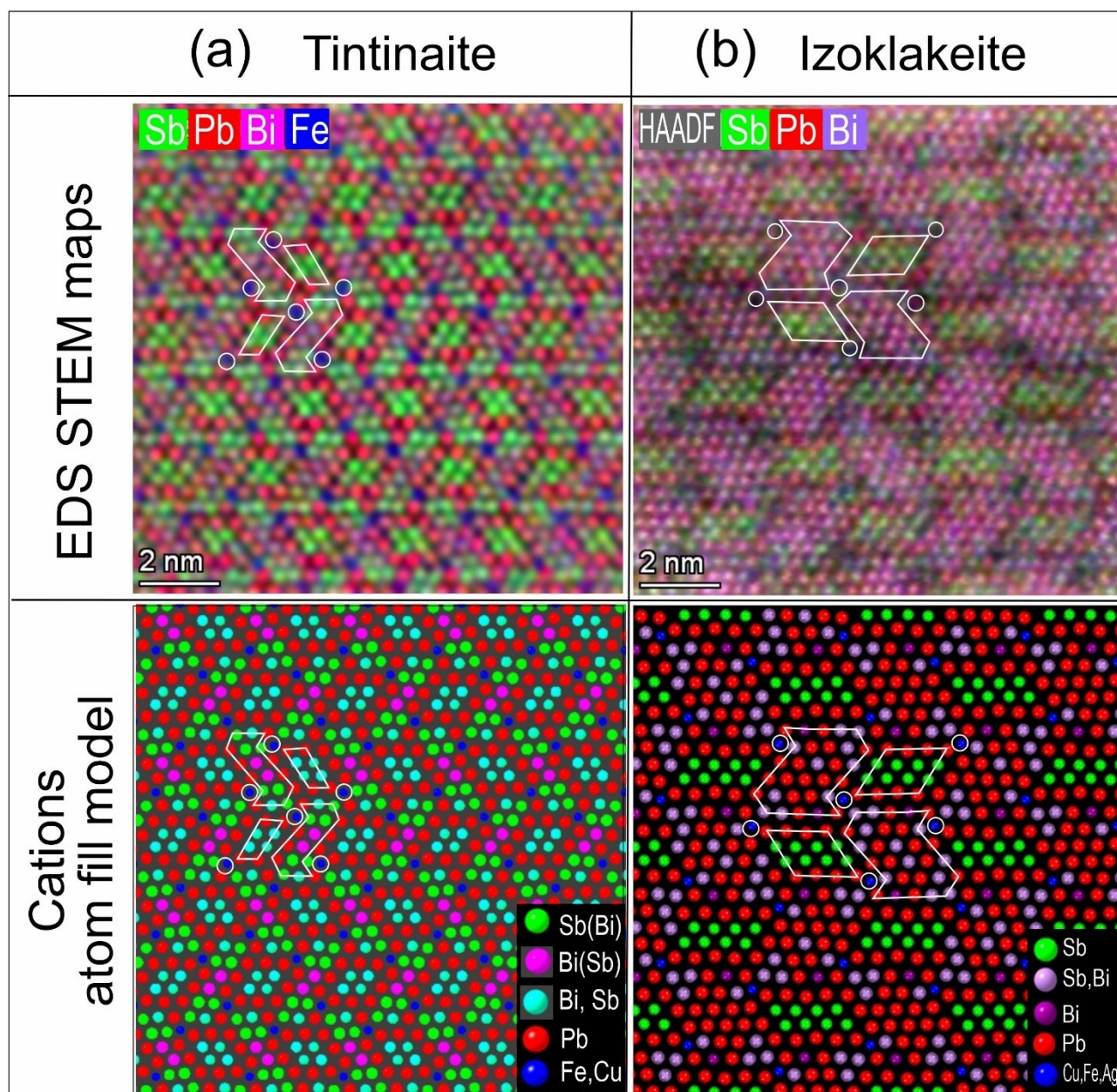
Ciobanu et al. Figure 6

**Figure 6.** High-resolution HAADF STEM images and corresponding fast Fourier transform (FFT) patterns for tintinaite (Tti) and izoklakeite (Iz) on [001] zone axis (labelled in square brackets). The SnS ( $n=8$  and  $16$  for Tti and Iz) and PbS ( $n=18$  and  $30$  for Tti and Iz) building modules are shown as overlays (green and red, respectively) highlighting the number of bright dots corresponding to heavier atoms; less brighter atoms at the corners of the modules are shown in yellow. The modules are depicted in (a) and (c) use the approach of Li *et al.* (2019) on the left, and Makovicky and Mumme (1986) on the right.



Ciobanu et al. Figure 7

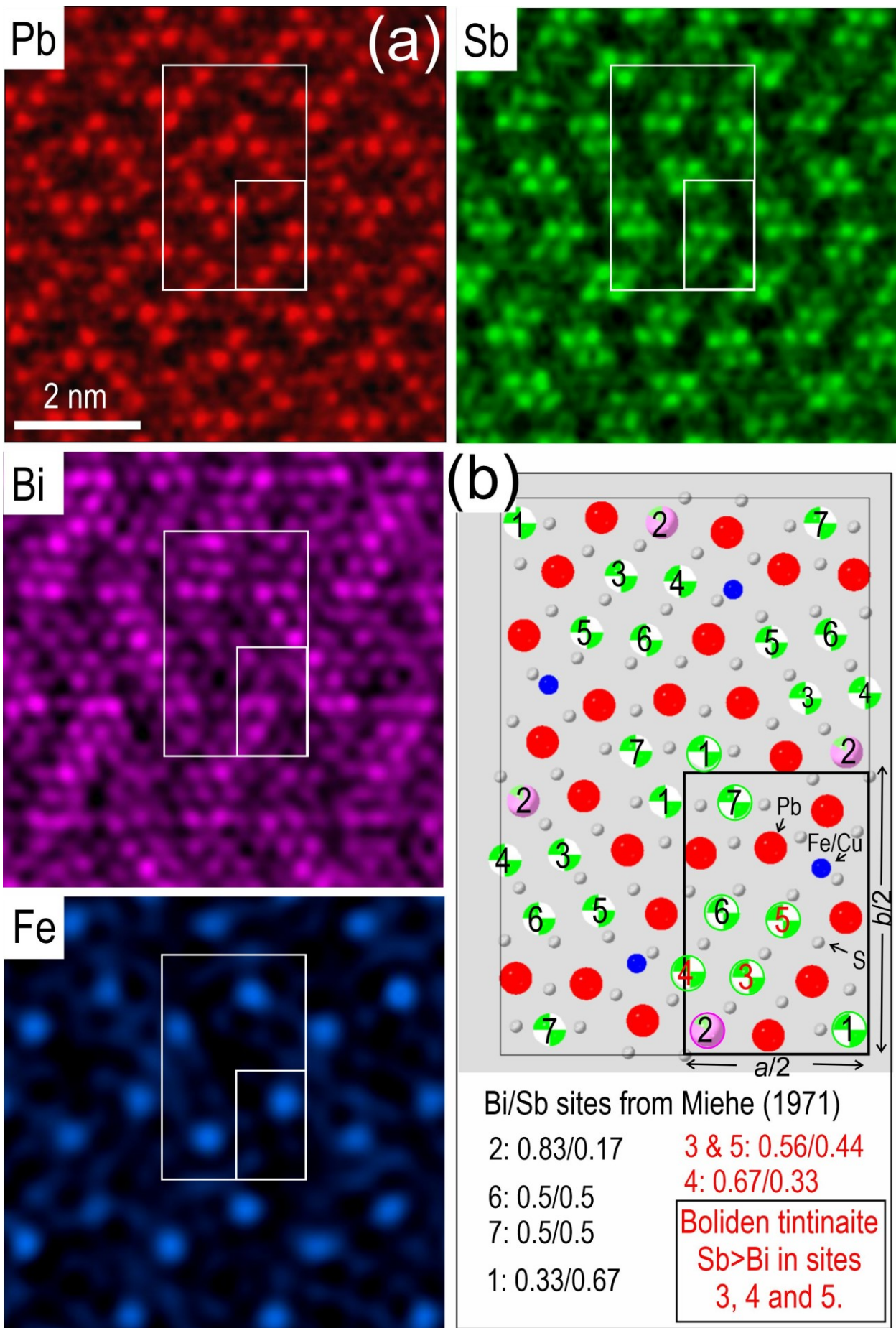
**Figure 7.** Crystal models, STEM simulations of kobellite and izoklakeite on [001] zone axis as labelled. Images for tintinaite and izoklakeite shown at the bottom of the figure. Simulations were obtained using the structures of Mieke (1971) and Makovicky and Mumme (1986) for kobellite and izoklakeite, respectively. The SnS and PbS building modules are highlighted by overlays. Weaker/longer Sb(Bi)-S bonds between adjacent polyhedra interpreted as lone electron pair micelles (e.g., Makovicky and Mumme, 1986) are marked by grey lines on atom-fill models. These correspond to dark lines on HAADF STEM images for tintinaite and izoklakeite and are highlighted by yellow lines across the overlays. Note that such features are visible through the middle of the SnS modules in izoklakeite, whereas in tintinaite they also occur through the PbS modules.



Ciobanu et al. Figure 8

**Figure 8.** Atomic resolution map overlays and models for tintinaite<sub>[001]</sub> and izoklakeite<sub>[001]</sub> as labelled. Extended element maps and additional overlays for tintinaite and izoklakeite are shown in Figures S2 and S3 (Supplementary Materials). Models were obtained using the structures of Mieke (1971) and Makovicky and Mumme (1986) for kobellite and izoklakeite, respectively. Note the match between the atomic arrangement and the building modules SnS and PbS shown as overlays. Circles show the atoms at the corners of these modules (Fe, Cu) and (Cu, Fe, Ag) for tintinaite and izoklakeite, respectively. Such atoms are exceptionally well depicted by the Fe maps for tintinaite.

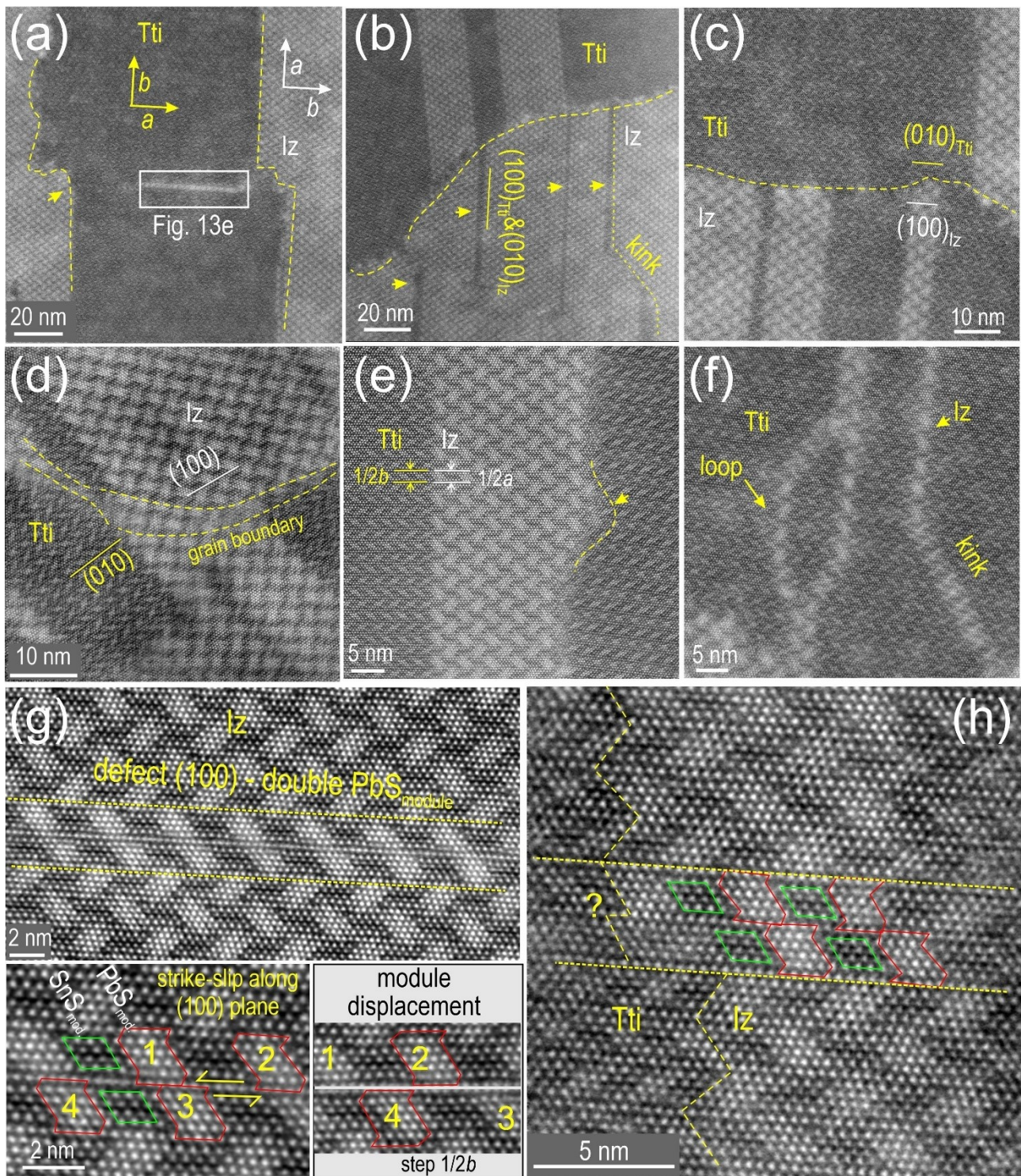
Prepublished Article



Ciobanu et al. Figure 9

**Figure 9.** (a) Element maps for Pb, Sb, Bi and Fe in tintinaite (crops from maps in Figure S2 Supplementary Material) showing the distribution of these elements throughout the structure whereby four Bi/Sb sites lie at the centre of the SnS modules; these are surrounded by Pb atoms. (b) Crystal model for the asymmetric unit cell of kobellite from Miehe (1971), there are seven Bi/Sb sites (labelled by numbers) of which two have 0.5/0.5 ratios, whereas the others, except site #1 where Sb is twice as much as Bi (0.33/0.67), have occupancies in which Bi>Sb. The map for Sb suggests, however, that occupancy is Sb>Bi for sites #3, 4 and 5. This is in agreement with the higher Sb/(Sb+Bi) ratio in Boliden tintinaite compared with the kobellite specimen studied by Miehe (1971); 66 mol.% and 44 mol.% tintinaite, respectively.

Prepublished Article

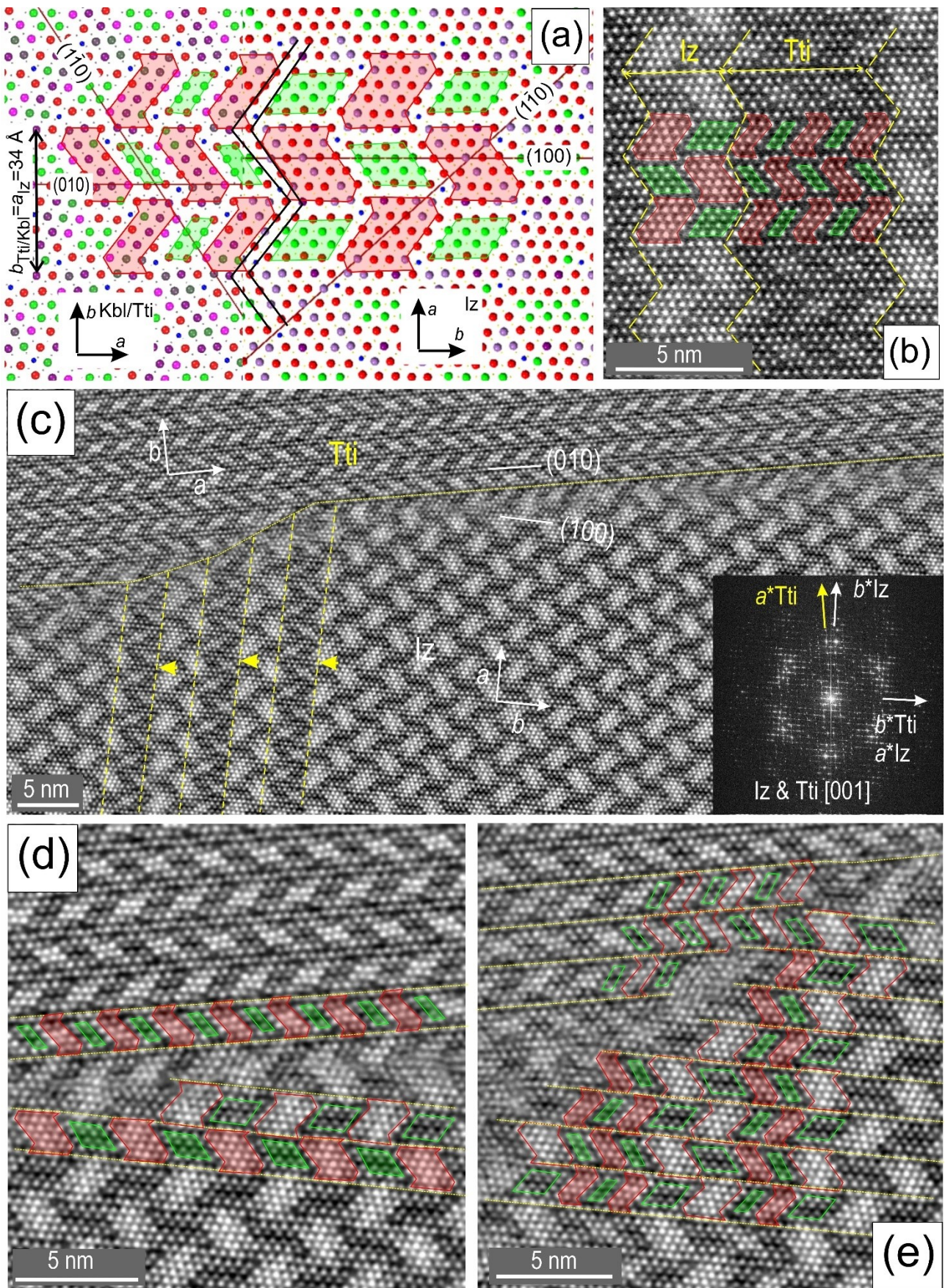


Ciobanu et al. Figure 10

**Figure 10.** (a-f) Images showing various types of intergrowths between tintinaite (Tti) and izoklakeite (Iz). (a) Tintinaite lamella with straight and irregular contacts (arrowed). (b, c) Curvilinear interfaces between grains with lamellar intergrowths of different thickness. Direction of planes for boundaries and intergrowths given in brackets. (d, e) At higher magnification, the grain boundary adjustments (dashed line) are illustrated by misorientations in the building modules (in d) and swells along boundaries (in e). (f) Loops and kinks are common along smallest arrays of one sulphosalt into another, in this case izoklakeite within tintinaite. (g)

Defect along (100) plane showing doubling of PbS modules in izoklakeite (image at the top). Underneath, left side, a detail showing the building modules (red outline for PbS (also numbered) and green for SnS) are shown to be displaced from one another along a strike-slip plane. At the edge (right side) of the defect, the displacement is by  $\frac{1}{2} b$  along the (100) plane. (h) Module displacement within izoklakeite affecting the contact with tintinaite.

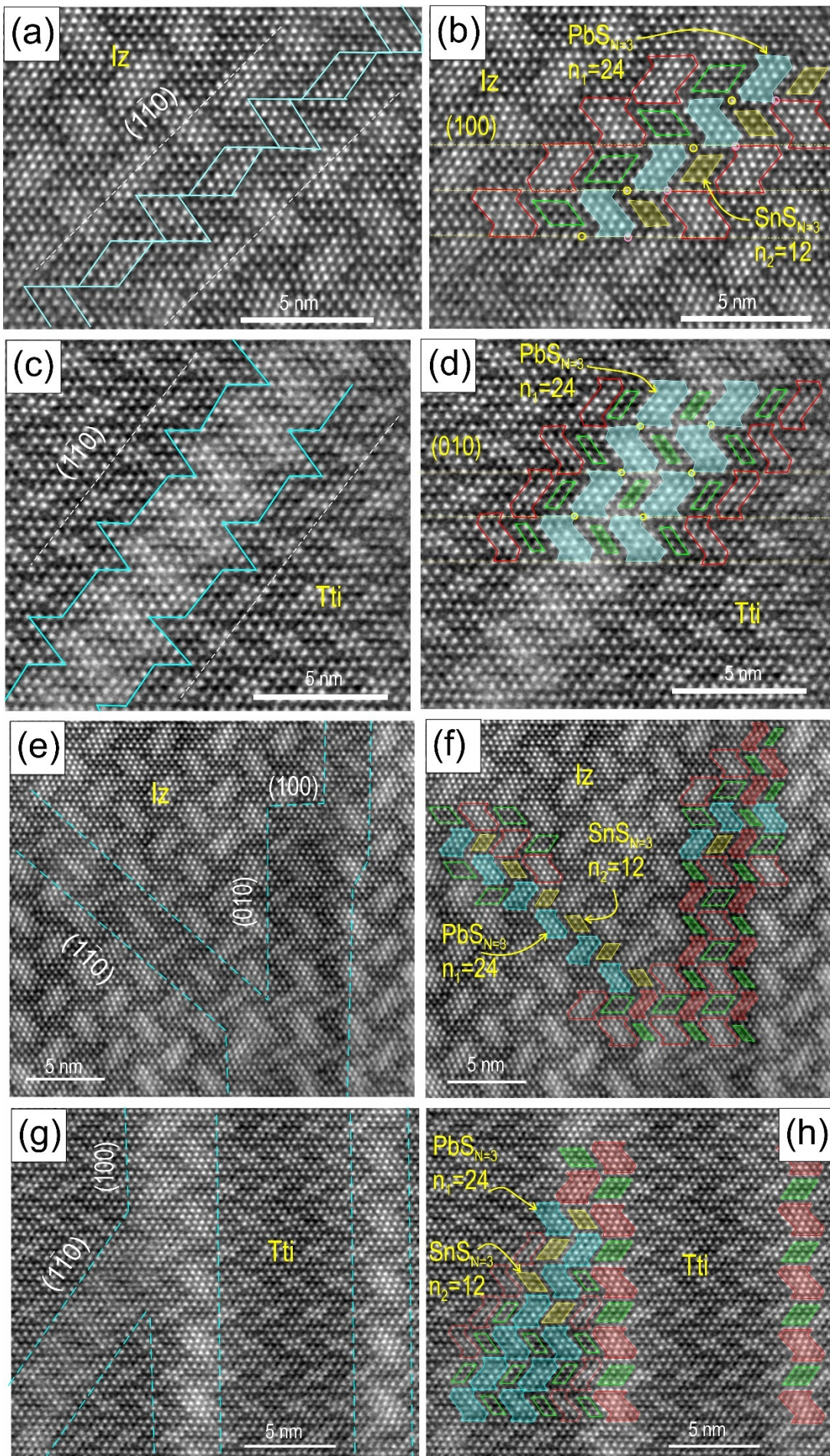
Prepublished Article



Ciobanu et al. Figure 11

**Figure 11.** Schematic model (a) and image (b) showing coherent contacts between izoklakeite (Iz) and tintinaite (Tti). PbS and SnS building modules are shown as red and green overlays. The match between  $b_{\text{Tti}}$  and  $a_{\text{Iz}}$  features alternating PbS and SnS modules that form a zig-zag line. (c) An oblique contact between  $[001]_{\text{Tti}}$  and  $[001]_{\text{Iz}}$ . Parallel arrays of tintinaite within izoklakeite are arrowed. The misalignment  $a^*_{\text{Tti}}$  and  $b^*_{\text{Iz}}$  is also shown in the FFT (inset). (d, e) Alignment between  $(010)_{\text{Tti}}$  and  $(100)_{\text{Iz}}$  planes features small-scale areas of mismatch, recognisable by misfit of the two types of modules and their respective morphologies.

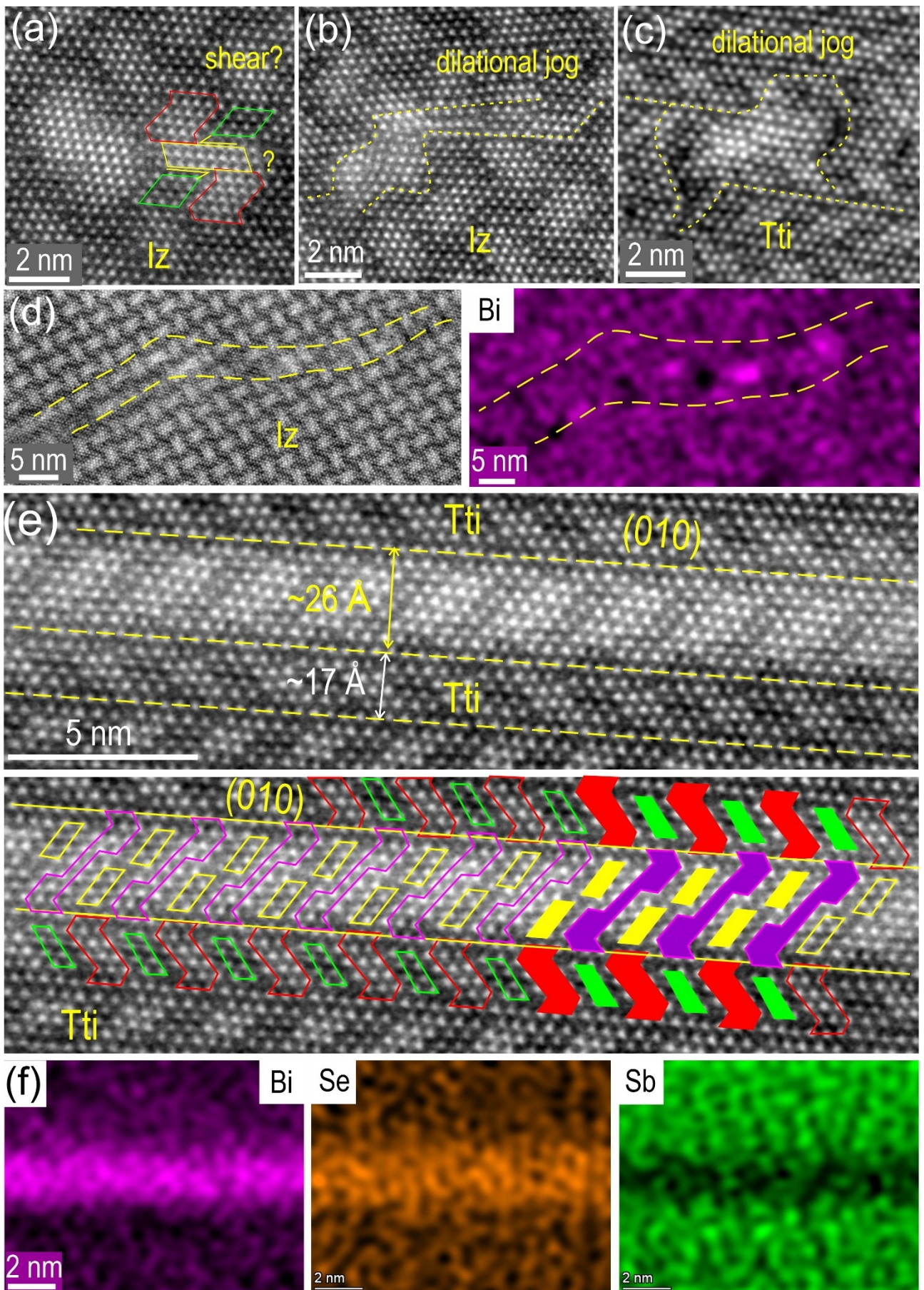
Prepublished Article



Ciobanu et al. Figure 12

**Figure 12.** (a, d) Single and double arrays of modular intergrowths in izoklakeite (Iz) and tintinaite (Tti) along planes from the  $\langle 110 \rangle$  family showing PbS ( $n=24$ ; blue) and SnS ( $n=12$ ; yellow) modules corresponding to the  $N=3$  homologue. Circles represent dots/atoms unaccounted for. (a, b) A single array (blue line in (a)) of the  $N=3$  homologue shown as  $\text{PbS}_{N3}$  (blue)- $\text{SnS}_{N3}$  (yellow) modules within izoklakeite ( $\text{PbS}_{\text{Iz}}$  and  $\text{SnS}_{\text{Iz}}$  modules outlined in red and green). (c, d) A double array (blue line in (c)) of  $\text{PbS}_{N3}$  modules intergrown with  $\text{SnS}_{\text{Tti}}$  modules in tintinaite. (e-h) Module disorder involving slabs of  $N=3$  homologue in intergrowths comprising changes in thickness or branching between arrays of different orientations as labelled in izoklakeite and tintinaite.

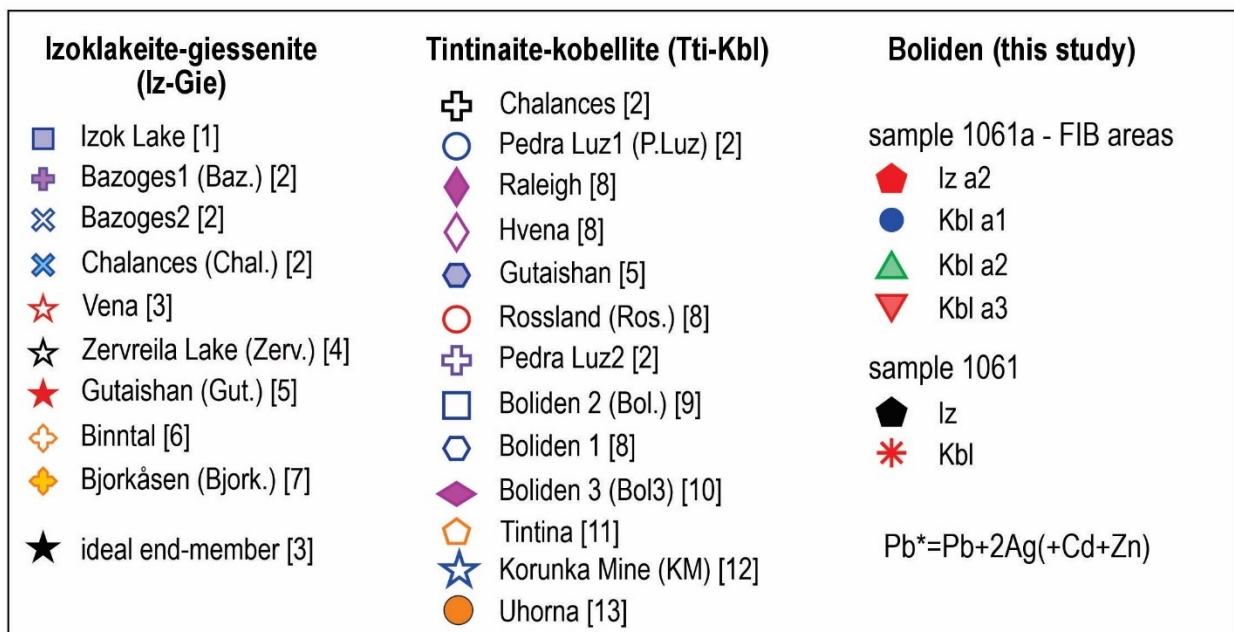
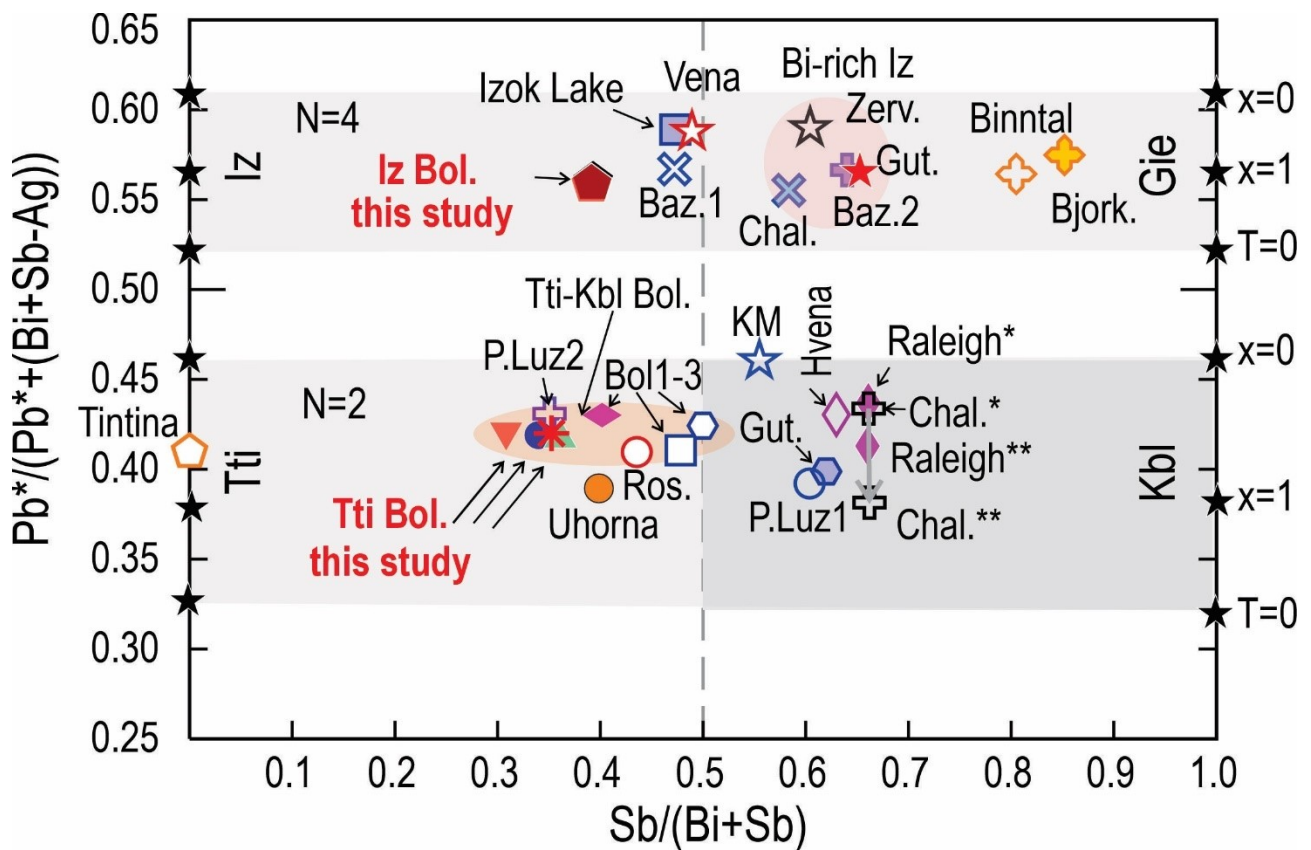
Prepublished Article



Ciobanu et al. Figure 13

**Figure 13.** Defects and textures crosscutting the main crystal structural motifs of the two sulphosalts and leading to redistribution of Bi and Se in izoklakeite (Iz) and tintinaite (Tti). (a) S-shaped defect derived from modification of PbS modules (red outline) in izoklakeite attributable to shear-displacement along  $(100)_{Iz}$  planes. SnS<sub>Iz</sub> module outlined in green. Note a slab of  $n=24$  dots/atoms of equal intensity with the PbS<sub>Iz</sub> along the displacement plane. (b, c) Defects showing irregular aggregation of PbS modules that are interpreted as dilational jogs in izoklakeite and tintinaite. (d) Nanoscale fracture in izoklakeite displaying Bi remobilization. (e) Image showing a  $\sim 26$  Å-wide lamella featuring building modules, which, although syntactic with host tintinaite, are different to kobellite homologues. A possible interpretation of the modules along the lamellae are given as overlays underneath the image. The SnS and PbS modules in tintinaite are also shown as green and red overlays. (f) EDS STEM maps of image in (e) showing localised enrichment in Bi and Se, and depletion in Sb.

Prepublished Article



Ciobanu et al. Figure 14

**Figure 14.** Diagram showing compositional variation in kobellite homologues from Boliden and comparison with other occurrences. Data from Tables 1-3 and Table S3 Supplementary Material. References: [1] Harris *et al.* (1986); [2] Mořlo *et al.* (1995); [3] Zakrzewski and Makovicky (1986); [4] Armbruster and Hummel (1987); [5] Li *et al.* (2019); [6] Graeser and Harris (1986); [7] Makovicky and Karup-Møller (1986); [8] Mořlo *et al.* (1984); [9] Mumme *et al.* (2013); [10] Wagner and Jonson (2001); [11] Harris *et al.* (1968); [12] Miehle (1971); [13] Prřek and Peterek (2008). See text for further explanation.

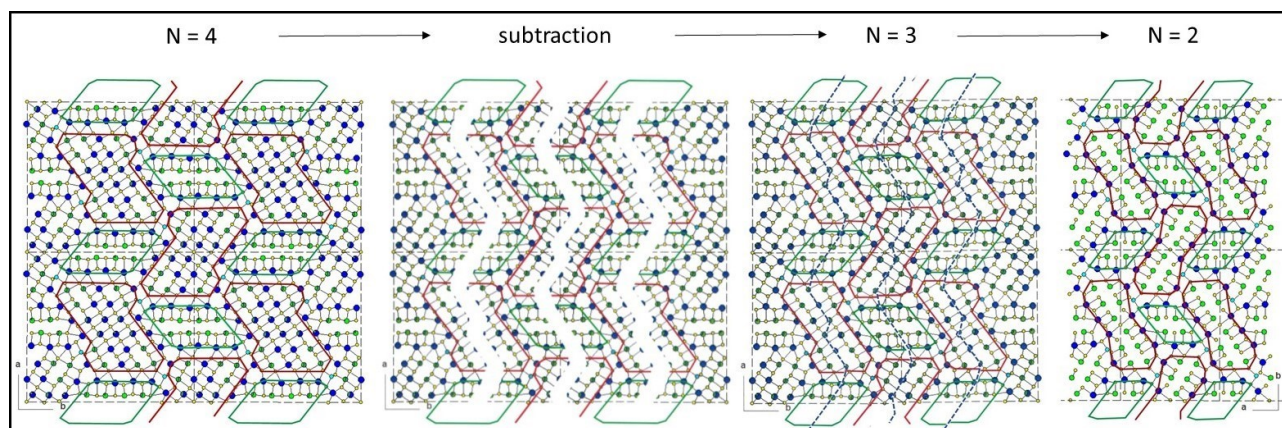


**Figure 15.** Proposed structure for the N=3 homologue. The structural formula (without Ag) can be considered as  $(\text{Cu}_{2-x}\text{Fe}_x)\text{Pb}_{18+x}(\text{Sb,Bi})_{18-x}\text{S}_{46}$ . Estimated unit cell parameters are  $a = 34.1 \text{ \AA}$ ,  $b = 41.5 \text{ \AA}$ , and  $c = 4.05 \text{ \AA}$ .

Prepublished Article

**Table 1.** Electron probe compositional data for izoklakeite

wt%	All (n=21)				Sample 1061 (n=8)				Sample 1061a (area 2) (n=13)			
	MEAN*	S.D.	MIN	MAX	MEAN	S.D.	MIN	MAX	MEAN	S.D.	MIN	MAX
Pb	<b>45.08</b>	0.35	44.35	45.58	44.73	0.20	44.35	45.04	45.30	0.23	44.93	45.58
Sb	<b>15.16</b>	0.25	14.52	15.49	14.97	0.30	14.52	15.27	15.28	0.11	15.05	15.49
Bi	<b>17.24</b>	0.28	16.69	17.95	17.40	0.29	16.95	17.95	17.13	0.22	16.69	17.49
Cu	<b>1.13</b>	0.03	1.08	1.18	1.12	0.02	1.08	1.15	1.14	0.03	1.09	1.18
Ag	<b>1.50</b>	0.10	1.32	1.72	1.46	0.11	1.32	1.60	1.53	0.09	1.42	1.72
Fe	<b>0.09</b>	0.01	0.07	0.11	0.09	0.01	0.07	0.10	0.10	0.01	0.08	0.11
Zn	<b>0.01</b>	0.01	<mdl	0.05	0.01	0.01	<mdl	0.02	0.01	0.01	<mdl	0.05
Cd	<b>0.01</b>	0.03	<mdl	0.09	0.02	0.03	<mdl	0.07	0.01	0.03	<mdl	0.09
S	<b>15.27</b>	0.12	15.06	15.49	15.17	0.08	15.06	15.32	15.34	0.09	15.21	15.49
Se	<b>4.82</b>	0.21	4.55	5.29	5.05	0.15	4.91	5.29	4.67	0.07	4.55	4.79
Te	<b>0.14</b>	0.06	0.08	0.27	0.22	0.03	0.16	0.27	0.10	0.01	0.08	0.13
Total	<b>100.3</b>	0.38	99.5	100.9	100.2	0.21	100.0	100.6	100.4	0.46	99.5	100.9
Formulae calculated @ 105 a.p.f.u.												
Pb	<b>22.92</b>	0.14	22.60	22.94	22.80	0.11	22.60	22.94	22.99	0.10	22.85	23.14
Sb	<b>13.12</b>	0.19	12.58	13.25	12.99	0.24	12.58	13.25	13.20	0.07	13.08	13.30
Bi	<b>8.69</b>	0.14	8.46	9.10	8.80	0.16	8.57	9.10	8.62	0.08	8.46	8.74
Ag	<b>1.47</b>	0.10	1.30	1.56	1.43	0.10	1.30	1.56	1.49	0.09	1.39	1.69
Cu	<b>1.88</b>	0.04	1.80	1.92	1.86	0.04	1.80	1.92	1.89	0.04	1.81	1.95
Fe	<b>0.18</b>	0.02	0.13	0.19	0.16	0.02	0.13	0.19	0.18	0.02	0.15	0.21
Zn	<b>0.01</b>	0.02	0.00	0.04	0.01	0.02	0.00	0.04	0.01	0.02	0.00	0.07

Cd	<b>0.01</b>	0.03	0.00	0.06	0.02	0.03	0.00	0.06	0.01	0.03	0.00	0.08
S	<b>50.19</b>	0.23	49.74	50.43	49.99	0.23	49.74	50.43	50.30	0.12	50.10	50.49
Se	<b>6.43</b>	0.30	6.06	7.10	6.76	0.20	6.56	7.10	6.22	0.10	6.06	6.37
Te	<b>0.12</b>	0.05	0.07	0.23	0.18	0.03	0.13	0.23	0.08	0.01	0.07	0.10
Ev (%)	<b>1.35</b>	0.66	-0.42	1.23	0.69	0.54	-0.42	1.23	1.75	0.31	1.07	2.03
End-member proportions												
% Iz Sb/(Bi+Sb)	<b>60</b>	0.70	58.2	60.7	60	0.85	58.2	60.7	60	0.28	59.9	61.0
% Gie Bi/(Bi+Sb)	<b>40</b>	0.70	39.0	41.8	40	0.85	39.3	41.8	40	0.28	39.0	40.1
Cu+Fe	<b>2.06</b>	0.05	1.94	2.08	2.0	0.05	1.9	2.08	2.1	0.05	2.0	2.14
Pb+2*Ag+Cd+Zn	<b>25.88</b>	0.20	25.57	25.93	25.7	0.14	25.6	25.93	26.0	0.14	25.8	26.29
Bi+Sb-Ag	<b>20.34</b>	0.11	20.14	20.45	20.3	0.09	20.2	20.45	20.3	0.12	20.1	20.52
Total M	<b>48.27</b>	0.19	47.81	48.25	48.1	0.15	47.8	48.25	48.4	0.08	48.2	48.50
S+Se+Te	<b>56.73</b>	0.19	56.50	57.19	56.9	0.15	56.8	57.19	56.6	0.08	56.5	56.78
N homologue	<b>3.83</b>	0.05	3.76	3.85	3.80	0.03	<b>3.8</b>	<b>3.85</b>	<b>3.85</b>	0.05	<b>3.8</b>	<b>3.94</b>

\*Weighted mean

**Table 2.** Electron probe compositional data for tintinaite

wt%	MEAN	All (n=47)			sample 1061 (n=15)				sample 1061a (areas 1-3) (n=32)			
		S.D.	MIN	MAX	MEAN	S.D.	MIN	MAX	MEAN	S.D.	MIN	MAX
Pb	<b>37.18</b>	0.70	36.07	38.36	<b>36.43</b>	0.28	36.07	36.87	<b>37.53</b>	0.53	36.58	38.36
Sb	<b>21.06</b>	0.82	19.89	22.42	<b>20.43</b>	0.54	19.89	21.39	<b>21.36</b>	0.77	20.29	22.42
Bi	<b>18.54</b>	1.29	16.61	20.53	<b>19.38</b>	0.94	17.96	20.53	<b>18.14</b>	1.26	16.61	20.03
Cu	<b>1.41</b>	0.06	1.30	1.54	<b>1.43</b>	0.03	1.38	1.49	<b>1.40</b>	0.06	1.30	1.54
Ag	<b>0.32</b>	0.05	0.21	0.44	<b>0.34</b>	0.02	0.31	0.39	<b>0.31</b>	0.05	0.21	0.44
Fe	<b>0.70</b>	0.05	0.61	0.79	<b>0.66</b>	0.03	0.61	0.74	<b>0.72</b>	0.05	0.63	0.79
Zn	<b>0.02</b>	0.02	<mdl	0.06	<b>0.03</b>	0.01	<mdl	0.05	<b>0.02</b>	0.02	<mdl	0.06
Cd	<b>0.10</b>	0.09	0.00	0.38	<b>0.10</b>	0.03	0.04	0.16	<b>0.11</b>	0.11	0.00	0.38
S	<b>17.52</b>	0.16	17.19	17.82	<b>17.34</b>	0.10	17.19	17.56	<b>17.61</b>	0.10	17.46	17.82
Se	<b>3.30</b>	0.11	3.03	3.53	<b>3.37</b>	0.15	3.03	3.53	<b>3.27</b>	0.06	3.13	3.36
Te	<b>0.01</b>	0.02	<mdl	0.12	<b>0.01</b>	0.01	<mdl	0.04	<b>0.01</b>	0.02	<mdl	0.12

Total	<b>100.2</b>	0.61	98.7	101.2	<b>99.5</b>	0.36	98.74	99.96	<b>100.5</b>	0.44	99.5	101.2
Formulae calculated @ 63 a.p.f.u.												
Pb	<b>10.58</b>	0.12	10.38	10.80	<b>10.46</b>	0.07	10.38	10.59	<b>10.63</b>	0.10	10.45	10.80
Sb	<b>10.20</b>	0.33	9.73	10.69	<b>9.99</b>	0.25	9.73	10.36	<b>10.30</b>	0.32	9.82	10.69
Bi	<b>5.23</b>	0.40	4.63	5.85	<b>5.52</b>	0.27	5.12	5.85	<b>5.10</b>	0.38	4.63	5.65
Ag	<b>0.18</b>	0.03	0.11	0.24	<b>0.19</b>	0.01	0.17	0.21	<b>0.17</b>	0.03	0.11	0.24
Cu	<b>1.31</b>	0.06	1.20	1.43	<b>1.34</b>	0.03	1.29	1.40	<b>1.29</b>	0.06	1.20	1.43
Fe	<b>0.74</b>	0.05	0.65	0.82	<b>0.70</b>	0.03	0.65	0.79	<b>0.76</b>	0.05	0.66	0.82
Zn	<b>0.02</b>	0.02	0.00	0.05	<b>0.02</b>	0.01	0.00	0.04	<b>0.02</b>	0.02	0.00	0.05
Cd	<b>0.05</b>	0.05	0.00	0.20	<b>0.05</b>	0.02	0.02	0.08	<b>0.06</b>	0.06	0.00	0.20
S	<b>32.22</b>	0.09	31.99	32.43	<b>32.18</b>	0.12	31.99	32.43	<b>32.25</b>	0.06	32.15	32.37
Se	<b>2.46</b>	0.09	2.28	2.67	<b>2.54</b>	0.11	2.28	2.67	<b>2.43</b>	0.04	2.34	2.49
Te	<b>0.00</b>	0.01	0.00	0.05	<b>0.00</b>	0.01	0.00	0.02	<b>0.00</b>	0.01	0.00	0.05
Ev (%)	<b>1.69</b>	0.39	0.35	2.14	<b>1.55</b>	0.49	0.35	2.01	<b>1.75</b>	0.31	0.93	2.14
End-member proportions												
%Tl Sb/(Bi+Sb)	<b>66</b>	2.43	62.6	69.6	<b>64</b>	1.69	62.6	66.9	<b>67</b>	2.33	63.6	69.6
%Kbl Bi/(Bi+Sb)	<b>34</b>	2.43	30.4	37.4	<b>36</b>	1.69	33.1	37.4	<b>33</b>	2.33	30.4	36.4
Cu+Fe	<b>2.05</b>	0.03	1.97	2.13	<b>2.0</b>	0.02	2.01	2.09	<b>2.05</b>	0.04	1.97	2.13
Pb+2*Ag+Cd+Zn	<b>11.01</b>	0.12	10.81	11.22	<b>10.9</b>	0.07	10.81	11.04	<b>11.05</b>	0.11	10.85	11.22
Bi+Sb-Ag	<b>15.26</b>	0.08	15.12	15.47	<b>15.3</b>	0.08	15.16	15.47	<b>15.23</b>	0.07	15.12	15.41
Total M	<b>28.31</b>	0.06	28.11	28.38	<b>28.3</b>	0.07	28.11	28.36	<b>28.32</b>	0.05	28.21	28.38
S+Se+Te	<b>34.69</b>	0.06	34.62	34.89	<b>34.7</b>	0.07	34.64	34.89	<b>34.68</b>	0.05	34.62	34.79
N homologue	<b>2.05</b>	0.02	<b>2.00</b>	<b>2.08</b>	<b>2.03</b>	0.02	2.00	2.06	<b>2.05</b>	0.02	<b>2.01</b>	<b>2.08</b>

**Table 3.** Electron probe compositional data for tinnite in three areas of sample 1061a, highlighting local variation

wt%	n=9	area2			n=8	area 1			n=15	area 3		
		S.D.	MIN	MAX		S.D.	MIN	MAX		S.D.	MIN	MAX
Pb	36.92	0.26	36.58	37.30	37.42	0.30	37.05	37.86	37.96	0.31	37.41	38.36
Sb	20.40	0.07	20.29	20.51	21.02	0.21	20.72	21.30	22.12	0.12	21.95	22.42
Bi	19.78	0.25	19.30	20.03	18.57	0.30	18.19	18.99	16.93	0.19	16.61	17.29
Cu	1.48	0.03	1.45	1.54	1.38	0.02	1.36	1.42	1.355	0.03	1.30	1.40
Ag	0.34	0.05	0.28	0.44	0.32	0.04	0.26	0.37	0.284	0.04	0.21	0.34

Fe	0.66	0.02	0.63	0.68	0.75	0.02	0.71	0.77	0.748	0.02	0.71	0.79
Zn	0.03	0.02	<mdl	0.06	0.01	0.02	<mdl	0.04	0.024	0.02	<mdl	0.05
Cd	0.06	0.05	<mdl	0.10	0.03	0.04	<mdl	0.10	0.180	0.12	<mdl	0.38
S	17.55	0.07	17.47	17.66	17.54	0.06	17.46	17.64	17.69	0.07	17.55	17.82
Se	3.21	0.04	3.16	3.26	3.27	0.06	3.13	3.31	3.30	0.05	3.20	3.36
Te	<mdl		<mdl	<mdl	<mdl		<mdl	<mdl	0.011	0.03	<mdl	0.12
Total	100.4	0.53	99.5	101.0	100.3	0.32	100.0	100.8	100.6	0.42	99.8	101.2
Calculated formulae @ 63 a.p.f.u												
Pb	10.51	0.04	10.45	10.59	10.64	0.07	10.57	10.76	10.70	0.06	10.59	10.80
Sb	9.88	0.04	9.82	9.96	10.17	0.10	10.02	10.30	10.61	0.04	10.51	10.69
Bi	5.58	0.06	5.48	5.65	5.24	0.09	5.12	5.36	4.73	0.06	4.63	4.83
Ag	0.19	0.03	0.15	0.24	0.17	0.02	0.14	0.20	0.15	0.02	0.11	0.19
Cu	1.38	0.03	1.34	1.43	1.28	0.02	1.26	1.32	1.24	0.03	1.20	1.29
Fe	0.70	0.02	0.66	0.72	0.79	0.02	0.75	0.82	0.78	0.02	0.75	0.82
Zn	0.03	0.02	0.00	0.05	0.01	0.02	0.00	0.04	0.02	0.02	0.00	0.05
Cd	0.03	0.02	0.00	0.05	0.02	0.02	0.00	0.05	0.09	0.06	0.00	0.20
S	32.30	0.07	32.18	32.37	32.24	0.06	32.17	32.32	32.22	0.04	32.15	32.30
Se	2.40	0.03	2.36	2.44	2.44	0.04	2.34	2.47	2.44	0.03	2.37	2.49
Te	0.00	0.00	0.00	0.00	0.00	0.00	0.00	0.00	0.00	0.01	0.00	0.05
Ev (%)	1.58	0.47	0.93	2.02	1.73	0.30	1.32	2.14	1.85	0.13	1.53	2.01
End-member proportions												
%Tti [Sb/(Bi+Sb)]	<b>64</b>	0.30	63.6	64.4	<b>66</b>	0.58	65.2	66.8	<b>69</b>	0.29	68.6	69.6
%Kbl [Bi/(Bi+Sb)]	<b>36</b>	0.30	35.6	36.4	<b>34</b>	0.58	33.2	34.8	<b>31</b>	0.29	30.4	31.4
Cu+Fe	<b>2.1</b>	0.03	2.05	2.13	<b>2.1</b>	0.02	2.03	2.11	<b>2.0</b>	0.03	1.97	2.09
Pb+2*Ag+Cd+Zn	<b>10.9</b>	0.09	10.85	11.11	<b>11.0</b>	0.06	10.94	11.10	<b>11.1</b>	0.09	10.95	11.22
Bi+Sb-Ag	<b>15.3</b>	0.06	15.22	15.41	<b>15.2</b>	0.04	15.17	15.29	<b>15.2</b>	0.06	15.12	15.31
Total M	<b>28.3</b>	0.07	28.21	28.38	<b>28.3</b>	0.05	28.25	28.38	<b>28.3</b>	0.03	28.25	28.38
S+Se+Te	<b>34.7</b>	0.07	34.62	34.79	<b>34.7</b>	0.05	34.62	34.75	<b>34.7</b>	0.03	34.62	34.75
N homologue	<b>2.05</b>	0.02	<b>2.01</b>	<b>2.08</b>	<b>2.04</b>	0.01	<b>2.03</b>	<b>2.06</b>	<b>2.06</b>	0.02	<b>2.01</b>	<b>2.08</b>

**Table 4.** Calculated N values<sup>1</sup> for sulphosalts in this study compared with literature data.

	Calculated formula @ 63 a.p.f.u.	Ratio Tti:Kbl	Calculated formula @ 105 a.p.f.u.	Ratio Iz:Gie
<b>Tintinaite-kobellite</b>	<b>N<sub>H</sub> (=2)</b>		<b>Izoklakeite</b>	<b>N<sub>H</sub> (=4)</b>
Tintina Moëlo <i>et al.</i> (1984)	2.17	100:0	Boliden Bol 1061 (this study)	3.80 60:40
Boliden 1061a (this study)	2.05	67:33	Bol 1061a (this study)	3.85
Boliden 1061 (this study)	2.03	64:36	Izok Lake Harris <i>et al.</i> (1986)	4.17 53:47
Boliden 3 Wagner & Jonsson (2001)	2.09	59:41	Bazoges1 Moëlo <i>et al.</i> (1995)	4.01 53:47
Boliden 2 Mumme <i>et al.</i> (2013)	1.95	52:48	Vena Zakrzewski & Makovicky (1986)	4.14 51:49
Boliden1 Moëlo <i>et al.</i> (1984)	2.15	50:50	Les Chalanches Moëlo <i>et al.</i> (1995)	3.73 4.01* 42:58 3.82**
Pedra Luz2 Moëlo <i>et al.</i> (1995)	2.14	65:35	Lake Zervreila Armbruster & Hummel (1987)	4.54 4.08*** 40:60
Uhorna Prsek & Peterec (2008)	1.96	60:40	Bazoges2 Moëlo <i>et al.</i> (1995)	4.09 36:64
Rosslund Moëlo <i>et al.</i> (1995)	1.96	56:44	Guitaishan Li <i>et al.</i> (2019)	4.12 35:65
Korunka Mine Mische (1971)	2.32	44:56	<b>Giessenite</b>	<b>N<sub>H</sub> (=4)</b>
Pedra Luz1 Moëlo <i>et al.</i> (1995)	1.92	40:60	Binntal Graeser & Harris (1986)	3.98 19.5:80.5
Guitaishan Li <i>et al.</i> (2019)	2.02	39:61	Bjorkåsen Makovicky & Karup-Møller (1986)	4.19 15:85
Hvena Moëlo <i>et al.</i> (1984)	2.18	37:63		
Les Chalanches Moëlo <i>et al.</i> (1995)	2.25 2.61* 2.09**	34:66		
Raleigh Moëlo <i>et al.</i> (1984)	2.25 2.37* 2.12**	34:66		

<sup>1</sup>Calculations used the formula for the tintinaite-kobellite and izoklakeite-giessenite series given by Moëlo *et al.* (1995):

tintinaite-kobellite:  $(\text{Cu}_{2-x}\text{Fe}_x)[\text{Pb}_{10-2z+x}(\text{Ag,Cu})_z(\text{Sb}_{1-y}\text{Bi}_y)_{16+z-x}]_{\Sigma=26}\text{S}_{35}$ , with  $0 \leq x \leq 1$ ;  $0 \leq y \leq 0.67$ ;  $0 \leq z \leq 0.54$ , and izoklakeite-giessenite:  $(\text{Cu}_{2-x}\text{Fe}_x)[\text{Pb}_{26-2z+x}(\text{Ag,Cu})_z(\text{Sb}_{1-y}\text{Bi}_y)_{20+z-x}]_{\Sigma=46}\text{S}_{57}$ , with  $0 \leq x \leq 1$ ;  $0.44 \leq y \leq 0.85$ ;  $0 \leq z \leq 2.2$ , with addition of the following as indicated:

\* excess Cu on Pb

\*\* excess Cu on (Sb+Bi)

\*\*\*Ag incorporated on (Sb,Bi) sites